

Numerical aspects of Casimir energy computation in acoustic scattering

Timo Betcke^a, Alexander Strohmaier^b, Xiaoshu Sun^{a,*}

^a*Department of Mathematics, University College London, London, WC1E 6BT, UK*

^b*School of Mathematics, University of Leeds, Leeds, LS2 9JT, UK*

Abstract

Computing the Casimir force and energy between objects is a classical problem of quantum theory going back to the 1940s. Several different approaches have been developed in the literature often based on different physical principles. Most notably a representation of the Casimir energy in terms of determinants of boundary layer operators makes it accessible to a numerical approach. In this paper, we first give an overview of the various methods and what is known rigorously about the connection between them. We then present a new numerical scheme for the computation of the Casimir energy for large scale problems, which is based on the spectral properties of the block matrices for the boundary layer operators. This method allows for Casimir energy calculation for large-scale practical problems and significantly speeds up the computations in that case. We also discuss the connection to the Krein-spectral shift function and computational aspects.

Keywords: Krein spectral shift function, Casimir energy, Krylov subspace, inverse-free generalized eigenvalue problem, Bempp-cl

1. Introduction

Casimir interactions are forces between objects such as perfect conductors. Hendrik Casimir predicted and computed this effect in the special case of two planar conductors in 1948 using a divergent formula for the zero point energy and applying regularisation to it [1]. This resulted in the famous formula for the attractive Casimir force per unit area

$$F(a) = -\frac{1}{A} \frac{\partial \mathcal{E}}{\partial a} = -\frac{\hbar c \pi^2}{240 a^4},$$

between two perfectly conducting plates, where A is the cross-sectional area of the boundary plates and \mathcal{E} is the Casimir energy as computed from a zeta regularised mode sum. The result here is for the electromagnetic field which differs by a factor of two from the force resulting from a massless scalar field. This force was measured experimentally by Sparnaay about 10 years later [2] and the Casimir effect has since become famous for its intriguing derivation and its counterintuitive nature. In 1996, precision measurements of the Casimir force between the extended bodies were conducted by S.K. Lamoreaux [3] confirming the theoretical predictions including the corrections for realistic materials. From 2000 to 2008, the Casimir force has been measured in various experimental configurations, such as cylinder-cylinder [4], plate-plate [5], sphere-plate [6] and sphere-comb [7]. The presence of the Casimir force has also been quoted as evidence for the zero point energy of the vacuum having direct physical significance. The classical way to compute Casimir forces mimicks Casimir's original computation and is based on zeta function regularisation of the vacuum energy. This has been carried out for a number of particular geometric situations (see [8, 9, 10, 11, 12] and references therein). The derivations

*Corresponding author

URL: t.betcke@ucl.ac.uk (Timo Betcke), a.strohmaier@leeds.ac.uk (Alexander Strohmaier), xiaoshu.sun.18@ucl.ac.uk (Xiaoshu Sun)

are usually based on special functions and their properties and require explicit knowledge of the spectrum of the Laplace operator.

In 1960s, Lifshitz and collaborators extended and modified this theory to the case of dielectric media [13] gave derivations based on the stress energy tensor. It has also been realised by quantum field theorists (see e.g. [14, 13, 15, 16, 17]) with various degrees of mathematical rigour that the stress energy approach yields Casimir's formula directly without the need for renormalisation or artificial regularisation. This tensor is defined by comparing the induced vacuum states of the quantum field with boundary conditions and the free theory. Once the renormalised stress energy tensor is mathematically defined, the computation of the Casimir energy density becomes a problem of spectral geometry (see e.g. [18]). The renormalised stress energy tensor and its relation to the Casimir effect can be understood at the level of rigour of axiomatic algebraic quantum field theory. We note however that the computation of the local energy density is non-local and requires some knowledge of the spectral resolution of the Laplace operator, the corresponding problem of numerical analysis is therefore extremely hard.

Lifshitz and collaborators also offered an alternative description based on the van der Waals forces between molecules. The plates consist of a collection of atomic-scale electric dipoles randomly oriented in the absence of the external forcing field. Quantum and thermal fluctuations may make the dipoles align spontaneously, resulting in a net electric dipole moment. The dipoles in the opposite plate feel this field across the gap and align as well. The two net electric dipole moments make the two plates attract each other. This approach emphasizes the influence from the materials more than the fluctuations in the empty space between the plates.

Somewhat independently from the spectral approach determinant formulae based on the van der Waal's mechanism were derived by various authors. We note here Renne [19] who gives a determinant formula for the van der Waals force based on microscopic considerations. Various other authors give path-integral considerations based on considerations of surface current fluctuations [20, 21, 22, 23, 24, 25, 26, 27, 28]. The final formulae proved suitable for numerical schemes and were also very useful to obtain asymptotic formulae for Casimir forces for large and small separations. The mathematical relation between the various approaches remained unclear, with proofs of equality only available in special cases. A full mathematical justification of the determinant formulae as the trace of an operator describing the Casimir energy was only recently achieved in [29] for the scalar field and [30] for the electromagnetic field. It was also proved recently in [31] that the formulae arising from Zeta regularisation, from the stress energy tensor, and from the determinant of the single layer operator all give the same Casimir forces.

We will now describe the precise mathematical setting and review the theory. Let $\Omega \subset \mathbb{R}^d$ be a non-empty bounded open subset with Lipschitz boundary $\partial\Omega$, which is the union of connected open sets Ω_j , for $j = 1, \dots, N$. We assume that the complement $\mathbb{R}^d \setminus \Omega$ of Ω is connected and the closures of Ω_j are pairwise non-intersecting. We denote the N connected components of the boundary $\partial\Omega$ by $\partial\Omega_j$. We will think of the open set Ω as a collection of objects Ω_j placed in \mathbb{R}^d and will refer to them as *obstacles*.

Then, several unbounded self-adjoint operators densely defined in $L^2(\mathbb{R}^d)$ can be defined.

- The operator Δ is the Laplace operator with Dirichlet boundary conditions on $\partial\Omega$.
- For $j = 1, \dots, N$, the operator Δ_j is the Laplace operator with Dirichlet boundary conditions on $\partial\Omega_j$.
- The operator Δ_0 is the ‘free’ Laplace operator on \mathbb{R}^d with domain $H^2(\mathbb{R}^d)$.

These operators contain the dense set $C_0^\infty(\mathbb{R}^d \setminus \partial\Omega)$ in their domains. If $f : \mathbb{R} \rightarrow \mathbb{R}$ is a polynomially bounded function this set is also contained in the domain of the operators $f(\Delta^{\frac{1}{2}})$, $f(\Delta_j^{\frac{1}{2}})$, and $f(\Delta_0^{\frac{1}{2}})$, in particular the

operator

$$D_f = f(\Delta^{\frac{1}{2}}) - f(\Delta_0^{\frac{1}{2}}) - \left(\sum_{j=1}^N [f(\Delta_j^{\frac{1}{2}}) - f(\Delta_0^{\frac{1}{2}})] \right)$$

is densely defined. It was shown in [29] that under additional analyticity assumptions on f the operator D_f is bounded and extends by continuity to a trace-class operator on $L^2(\mathbb{R}^d)$. These analyticity assumptions are in particular satisfied by $f(\lambda) = (\lambda^2 + m^2)^{\frac{s}{2}}$ for any $s > 0, m \geq 0$ and one has

$$\text{Tr}(D_f) = \frac{s}{\pi} \sin\left(\frac{\pi}{2}s\right) \int_m^\infty \lambda(\lambda^2 + m^2)^{\frac{s}{2}-1} \Xi(i\lambda) d\lambda, \quad (1)$$

where the function Ξ is given by

$$\Xi(\lambda) = \log \det V_\lambda \tilde{V}_\lambda^{-1}$$

and the operators V_k and \tilde{V}_k are certain boundary layer operators that will be defined later. It was proved in [29] that this $V_\lambda \tilde{V}_\lambda^{-1} - 1$ near the positive imaginary axis is indeed a holomorphic family of trace-class operators on the Sobolev space $H^{\frac{1}{2}}(\partial\Omega)$ so that the above determinant is well-defined in the sense of Fredholm. We remark here that the paper [29] assumed the boundary to be smooth and the operators $V_\lambda \tilde{V}_\lambda^{-1}$ was considered as a map on $L^2(\partial\Omega)$. The main result of the paper also holds for Lipschitz boundaries if $L^2(\partial\Omega)$ is replaced by $H^{\frac{1}{2}}(\partial\Omega)$. This requires minor modifications of the proof but we will not discuss this further here, as we are now focusing on computational aspects.

We also recall that by the Birman-Krein formula we have for any even function $h \in \mathcal{S}(\mathbb{R})$ the equality

$$\text{Tr}\left(h(\Delta^{\frac{1}{2}}) - h(\Delta_0^{\frac{1}{2}}) - \left(\sum_{j=1}^N [h(\Delta_j^{\frac{1}{2}}) - h(\Delta_0^{\frac{1}{2}})]\right)\right) = \int_0^\infty h'(\lambda) \xi(\lambda) d\lambda, \quad (2)$$

where

$$\xi(\lambda) = \frac{1}{2\pi i} \log \left(\frac{\det(S(\lambda))}{\det(S_{1,\lambda}) \cdots \det(S_{N,k}(\lambda))} \right)$$

will be called the relative Krein spectral shift function. Here, $S_{j,k}$ are the scattering matrices of Δ_j associated to the objects Ω_j . Note here that the class of functions for which this is true can be relaxed to a certain extent, but even the most general version does not allow unbounded functions such as $f(\lambda)$ with $s > 0, m \geq 0$. The relative spectral shift function can however be related via a Laplace transform to the Fourier transform of the relative spectral shift function (see [32]). Under mild convexity assumptions this can be connected to the Duistermaat-Guillemin trace formula in obstacle scattering theory to give an asymptotic expansion of $\Xi(\lambda)$ in terms of the minimal distance $\delta > 0$ between the obstacles and the linearised Poincaré map of the bouncing ball orbits between the obstacles of that length. One has

$$\Xi(\lambda) = - \sum_j \frac{1}{|\det(I - P_{\gamma_j})|^{\frac{1}{2}}} e^{2i\delta\lambda} + o(e^{-2\delta\text{Im}\lambda}),$$

where the sum is over bouncing ball modes of length 2δ and P_{γ_j} is the associated Poincaré map, where γ_j is the shortest bouncing ball orbits.

The Casimir energy of the configuration Ω for a massless scalar field would then be given by D_f in the case when $f(\lambda) = \lambda$ and is therefore equal to

$$\mathcal{E} = -\frac{\hbar c}{2\pi} \int_0^\infty \Xi(i\lambda) d\lambda.$$

In this paper, we are going to introduce the numerical framework of computing the Casimir energy based on the evaluation of the log determinant of the integral operators in the acoustic case ¹ in Section 2 and discuss the

¹The mathematical theories and numerical experiments in the Maxwell case have been done as well and they will be reported in another paper.

spectral properties of the block matrices constructed from the integral operators in Section 3. Afterwards, with these properties, two efficient methods for computing the integrand of the Casimir energy will be illustrated in Section 4 which makes us compute the large-scale problem efficiently. In Section 5, several examples on computing the Casimir energy between the compact objects will be shown and we will also compare our results with others computed in other methods. Note that all the tests and examples in this paper were computed with version 0.2.4 of the Bempp-cl library [33]. Finally, Section 6 will conclude our paper and discuss the future plan as well.

2. Numerical methods for computing the Casimir energy in acoustic scattering

In this section, we give details of computing the Casimir energy via boundary integral operator discretisations. Assume $\Omega^- \in \mathbb{R}^d$, for $d \geq 2$ is the interior bounded Lebesgue-measurable domain that the scatterer occupies with piecewise smooth Lipschitz boundary Γ . The exterior domain is denoted as $\Omega^+ = \mathbb{R}^d \setminus \overline{\Omega^-}$. \mathbf{n} is the exterior unit normal to the surface Γ pointing outwards from Ω^- and \mathbf{n}_x is normal to Γ at the point $x \in \Gamma$.

In the scalar case, the Casimir energy can be expressed in terms of certain single-layer boundary operator, which we will define below. We then present its relationship with the Krein-Spectral shift function and demonstrate how it can practically be computed.

2.1. The single-layer boundary operator

For the bounded interior domain Ω^- or the unbounded exterior domain Ω^+ , the space of the (locally) square integrable functions is

$$L^2(\Omega^\pm) := \left\{ f : \Omega^\pm \rightarrow \mathbb{C}, f \text{ is Lebesgue measurable and } \int_{\Omega^\pm} |f|^2 < \infty \right\},$$

$$L_{\text{loc}}^2(\Omega^+) := \left\{ f : \Omega^+ \rightarrow \mathbb{C}, f \text{ is Lebesgue measurable and } \int_K |f|^2 < \infty, \text{ for all compact } K \subset \Omega^+ \right\}$$

and note that the subscript ‘‘loc’’ can be removed if the domain is bounded (i.e. $L_{\text{loc}}^2(\Omega^-) = L^2(\Omega^-)$). We define the (local) Sobolev space $H_{\text{loc}}^s(\Omega^\pm)$ as

$$H_{\text{loc}}^s(\Omega^\pm) := \left\{ f \in L_{\text{loc}}^2(\Omega^\pm), \forall \alpha \text{ s.t. } |\alpha| \leq s, D^\alpha f \in L_{\text{loc}}^2(\Omega^\pm) \right\},$$

where $\alpha = (\alpha_1, \alpha_2, \dots, \alpha_d)$ is a multi-index and $|\alpha| = \alpha_1 + \alpha_2 + \dots + \alpha_d$, and the derivative is defined in the weak sense.

For any function $f \in H_{\text{loc}}^1(\Omega)$ we can define the trace γ_D^\pm as

$$\gamma_D^\pm p(x) := \lim_{\Omega^\pm \ni x' \rightarrow x \in \Gamma} p(x').$$

We call the range of the trace operator $H^{1/2}(\Gamma)$. This space can be more rigorously defined. But for the purposes of this paper the description of $H^{1/2}(\Gamma)$ is range space of the trace operator is sufficient. We furthermore need the space $H^{-1/2}(\Gamma)$, which is the dual space of $H^{1/2}(\Gamma)$ with $L^2(\Gamma)$ as pivot space.

We can now define the single-layer boundary $\mathcal{V} : H^{-1/2}(\Gamma) \rightarrow H^{1/2}(\Gamma)$ as

$$(V_k \mu)(x) := \int_{\Gamma} g_k(x, y) \psi(y) dS_y, \quad \text{for } \mu \in H^{-\frac{1}{2}}(\Gamma) \text{ and } x \in \Gamma.$$

Here,

$$g_k(x, y) = \begin{cases} \frac{i}{4} H_0^{(1)}(k|x - y|), & \text{for } d = 2 \\ \frac{e^{ik|x-y|}}{4\pi|x-y|}, & \text{for } d = 3, \end{cases} \quad (3)$$

with $H_0^{(1)}$ a Hankel function of the first kind.

2.2. Relation between the Krein spectral shift function and the single-layer boundary operator

By [29], the Krein spectral shift function is defined as

$$\xi(k) = \frac{1}{2\pi i} \log \left(\frac{\det(S(k))}{\det(S_{1,k}) \cdots \det(S_{N,k})} \right),$$

where $S_{i,n}$ is the scattering matrix associated with the n th scatterer. These scattering matrices can be constructed $S_{i,n} = I + 2T_{i,n}$, where I is the identity matrix and $T_{i,n}$ is the T -matrix. The method of computing the T -matrix is fully discussed in [34] and [35].

The following theorem links the single-layer boundary operator with the Krein spectral shift function.

Theorem 1. [29] Consider Ω as a domain assembling from individual objects Ω_i . Let V_k be the single-layer boundary operator defined on the boundary $\partial\Omega = \bigcup_{i=1}^N \partial\Omega_i$, and \tilde{V}_k is the “diagonal part” of V_k by restricting the integral kernel to the subset $\bigcup_{i=1}^N \partial\Omega_i \times \partial\Omega_i \subset \partial\Omega \times \partial\Omega$ then the operator $V_k \tilde{V}_k^{-1}$ is trace-class and

$$\Xi(k) = \log \det(V_k \tilde{V}_k^{-1}).$$

Then for $k > 0$, we have

$$-\frac{1}{\pi} \operatorname{Im}\Xi(k) = \frac{i}{2\pi} (\Xi(k) - \Xi(-k)) = \xi(k)$$

and by choosing $h(x) = x$ in (2), this gives the formula

$$\operatorname{Tr} \left(\Delta^{\frac{1}{2}} + (N-1)\Delta_0^{\frac{1}{2}} - \sum_{i=1}^N \Delta_j^{\frac{1}{2}} \right) = \int_0^\infty \xi(k) dk = -\frac{1}{\pi} \int_0^\infty \Xi(ik) dk. \quad (4)$$

Equation (4) is used to compute the Casimir energy between the objects and the formula is written as

$$\mathcal{E} = \frac{\hbar c}{2} \int_0^\infty \xi(k) dk = -\frac{\hbar c}{2\pi} \int_0^\infty \Xi(ik) dk \quad (5)$$

Remark 1. Note that the integral $\frac{\hbar c}{2} \int_0^\infty \xi(k) dk$ in (5) is not Lebesgue convergent and requires regularisation for its numerical evaluation. The right-hand side integral does not suffer from this issue.

Corrected to here

2.3. Galerkin discretization and boundary element spaces

In order to compute the integral (5), we need to compute the log determinant of the operators $V_k \tilde{V}_k^{-1}$. In this section we discuss Galerkin discretisations to compute this quantity.

Define the triangulation \mathcal{T}_h of the boundary surface Γ with triangular surface elements τ_l and associated nodes \mathbf{x}_i s.t. $\overline{\mathcal{T}_h} = \bigcup_l \overline{\tau_l}$, where h is the mesh size and define the space of the continuous piecewise linear functions

$$P_h^1(\Gamma) = \{v_h \in C^0(\Gamma) : v_h|_{\tau_l} \in \mathbb{P}_1(\tau_l), \text{ for } \tau_l \in \mathcal{T}_h\},$$

where $\mathbb{P}_1(\tau_l)$ denotes the space of polynomials of order less than or equal to 1 on τ_ℓ . We have

$$P_h^1(\Gamma) := \operatorname{span}\{\phi_j\} \subset H^{-\frac{1}{2}}(\Gamma)$$

with

$$\phi_j(\mathbf{x}_i) = \begin{cases} 1, & i = j, \\ 0, & i \neq j \end{cases}$$

being the nodal basis functions.

Remark 2. Since $H^{-1/2}(\Gamma)$ does not require continuity we could use a space of simple piecewise constant functions. The reason why we choose piecewise linear functions is the size of the arising matrix systems for dense calculations. The computation of the log-determinant requires $\mathcal{O}(n^3)$ operations, where n is the dimension of our approximation basis. For sphere-like and other similar geometries there are in practice roughly twice as many triangles as nodes in the mesh. Hence, while the assembly cost with piecewise linear functions is higher, the resulting matrix has only half the dimension, resulting in roughly a factor eight reduction of computational complexity for the log determinant. A disadvantage is that on geometries with corners or edges the converges close to these singularities is suboptimal with continuous piecewise linear functions.

Having defined the basis function ϕ_j , we can represent each element inside the Galerkin discretization form. Assume there are N objects, then the matrix of the operator V_k is an N by N block matrix, written as

$$V(k) = \begin{bmatrix} V_{11}(k) & V_{12}(k) & \cdots & V_{1N}(k) \\ V_{21}(k) & V_{22}(k) & \cdots & V_{2N}(k) \\ \vdots & \vdots & \ddots & \vdots \\ V_{N1}(k) & V_{N2}(k) & \cdots & V_{NN}(k) \end{bmatrix} \quad (6)$$

and the matrix \tilde{V}_k is the diagonal part of V_k :

$$\tilde{V}(k) = \begin{bmatrix} V_{11}(k) & 0 & \cdots & 0 \\ 0 & V_{22}(k) & \cdots & 0 \\ \vdots & \vdots & \ddots & \vdots \\ 0 & 0 & \cdots & V_{NN}(k) \end{bmatrix}. \quad (7)$$

Therefore, the element in the m th row and n th column of the block matrix $V_{ij}(k)$ is

$$V_{ij}^{(m,n)}(k) = \langle V_{ij}(k)\phi_m^{(i)}, \phi_n^{(j)} \rangle = \int_{\Gamma} \overline{\phi_n^{(j)}(\mathbf{x})} \int_{\Gamma} g_k(\mathbf{x}, \mathbf{y}) \phi_m^{(i)}(\mathbf{y}) dS_{\mathbf{y}} dS_{\mathbf{x}}, \quad (8)$$

where $\phi^{(i)} = [\phi_1^{(i)} \quad \phi_2^{(i)} \quad \dots \quad \phi_N^{(i)}]$ is the set of basis functions defined on the i th object and

$$\langle f, g \rangle = \int_{\Gamma} f(\mathbf{x}) \overline{g(\mathbf{x})} dS_{\mathbf{x}}$$

denotes the standard $L^2(\Gamma)$ inner product.

The value of $\Xi(ik) = \log \det(V(ik)\tilde{V}(ik)^{-1})$ can now be explicitly computed by evaluating the corresponding log determinants.

The function $\Xi(ik)$ has a very favourable decay behaviour for growing k that we can use to limit the number of quadrature points necessary to evaluate the corresponding Casimir integral, namely under certain convexity assumptions on the obstacles it holds that

$$\Xi(ik) = \mathcal{O}(e^{-2Zk}).$$

Here, Z is the minimum distance between the obstacles [36, Theorem 4.1].

This result can be justified heuristically, using a simple matrix perturbation argument. Consider a symmetric matrix A partitioned as

$$A = \begin{bmatrix} A_1 & 0 \\ 0 & A_2 \end{bmatrix}.$$

and a symmetric matrix E partitioned as

$$E = \begin{bmatrix} 0 & E_1^T \\ E_1 & 0 \end{bmatrix}$$

Then it holds for the i th eigenvalue $\lambda_i(A)$ and the i th eigenvalue $\lambda_i(A + E)$ that

$$|\lambda_i(A) - \lambda_i(A + E)| \leq \frac{\|E\|^2}{\text{gap}_i},$$

where gap_i is the distance of $\lambda_i(A)$ to the spectrum of A_2 if $\lambda_i(A)$ is an eigenvalue of A_1 , and to the spectrum of A_1 if $\lambda_i(A)$ is an eigenvalue of A_2 . Details can be found in [37] [The reference to Roy Matthias is suddenly missing.](#)

Now assume that we have two different obstacles. Then we have $A_1 = V_{11}(k)$, $A_2 = V_{22}(k)$ and $E_1 = V_{21}$ as the matrix of cross interactions between the two obstacles. The Green's function between two obstacles decays exponentially like e^{-Zk} , where Z is the minimal distance between them, resulting in a matrix perturbation result of the form $|\lambda_i(V) - \lambda_i(\tilde{V})| = O(e^{-2Zk})$ for increasing k , from which the corresponding perturbation result for the log determinant follows.

This purely linear algebraic consideration is not fully robust as it ignores the importance of the eigenvalue gap in the perturbation result. But we can heuristically explain the gap as follows. On the continuous level the perturbations E_1 and E_2 are compact, so the tail end of the spectrum that converges to zero with small values of gap_i , is little effected by E , and the corresponding eigenvalues have a contribution of $\log \left| \frac{\lambda_i(A)}{\lambda_i(A+E)} \right| \approx 0$ to the value of Ξ . The relevant eigenvalues are the larger ones who for distinct obstacles have a sufficiently large value of gap_i .

While the linear algebra argument is useful to give a heuristical explanation, it is not as rigorous as the analytical result in [36]. In particular, we want to emphasize that the exponential decay bound with the quadratic factor also holds if the two obstacles are identical, which is not obvious from pure linear algebraic considerations. An example of this is given in Figure 1.

The integrand value of Casimir integral formula

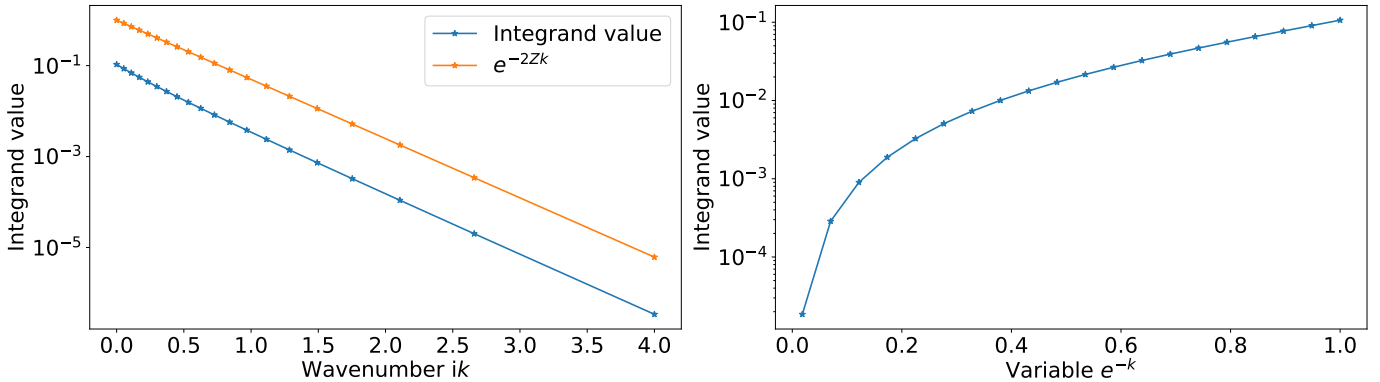


Figure 1: (Left) Exponential decay of $\Xi(ik)$ for two identical spheres with radius $R = 1$ and minimum distance $Z = 1.5$. The red line is the decay bound and the blue line is the actual decay. (Right). The integrand $\Xi(ik)$ after variable transformation to apply a numerical trapezoid rule for its evaluation.

This nice numerical property for the integrand $\Xi(ik)$ simplifies the numerical integration. One can apply the normal trapezoidal rule to calculate the integral $\int_0^\infty \Xi(ik) dk = \int_0^\infty \log \frac{\det V(ik)}{\det \tilde{V}(ik)} dk$ with k changed to y with $y = e^{-k}$. Figure 1 (Right) plots the integrand with regard to the new variable y .

3. Spectral property of the integral operators

The matrix M_∞ is a compact perturbation of matrix M , which makes the eigenvalues of them close to each other. Therefore, if we plot the eigenvalues of the matrix MM_∞^{-1} , we can notice that there are many eigenvalues closed to 1 and nearly contributes nothing to the log determinant. This spectral property inspires us to use

some iteration method to approximate the extreme eigenvalues of MM_{∞}^{-1} . In order to make the computation process more efficiently, we will introduce an inverse-free method to speed up this process which makes us deal with the large-scale problem in the future.

4. Efficient methods for computing $\log \det(\mathbf{V}_{ik}\tilde{\mathbf{V}}_{ik}^{-1})$

By Section 2, to compute the Casimir energy, it is necessary to evaluate the term $\log \frac{\det \mathbf{V}_{ik}}{\det \tilde{\mathbf{V}}_{ik}} = \log \det(\mathbf{V}_{ik}\tilde{\mathbf{V}}_{ik}^{-1})$ with different values of k . In this section, several efficient methods will be introduced to compute this log determinant.

The log determinant of the matrix $\mathbf{V}_{ik}\tilde{\mathbf{V}}_{ik}^{-1}$ is equal to the sum of the logarithm of the eigenvalues of $\mathbf{V}_{ik}\tilde{\mathbf{V}}_{ik}^{-1}$. Since $\tilde{\mathbf{V}}_{ik}$ is a compact perturbation of \mathbf{V}_{ik} , most of the eigenvalues of the matrix $\mathbf{V}_{ik}\tilde{\mathbf{V}}_{ik}^{-1}$ are close to 1 (shown in the Figure 2) and contribute little on the value of Casimir energy. Therefore, the computation process for the large-scale problem can become efficient if only multiple extreme eigenvalues that mainly contribute to the log determinant are computed. In addition, we should also avoid directly computing the inverse of the matrix $\tilde{\mathbf{V}}_{ik}$ since the computational complexity is cubic with respect to the matrix dimension.

In what follows, one method called inverse-free Krylov subspace method will be introduced to compute multiple extreme eigenvalues. For each quadrature point k_j , $j = 1, \dots, N$, one can directly apply this method to find the log determinant of $\mathbf{V}_{ik_j}\tilde{\mathbf{V}}_{ik_j}^{-1}$. However, by recalling Figure 1, most of the quadrature points are closed to each other, which inspires us to recycle the subspace obtained from $\mathbf{V}_{ik_j}\tilde{\mathbf{V}}_{ik_j}^{-1}$ and use it for $\mathbf{V}_{ik_{j+1}}\tilde{\mathbf{V}}_{ik_{j+1}}^{-1}$'s case. Afterwards, another efficient method based on the standard Arnoldi iterations will be demonstrated and its corresponding recycling-subspace-based method will be discussed as well. Finally, the comparison of among these methods on their performance for approximating the log determinant and the number of matrix-vector multiplications will be shown.

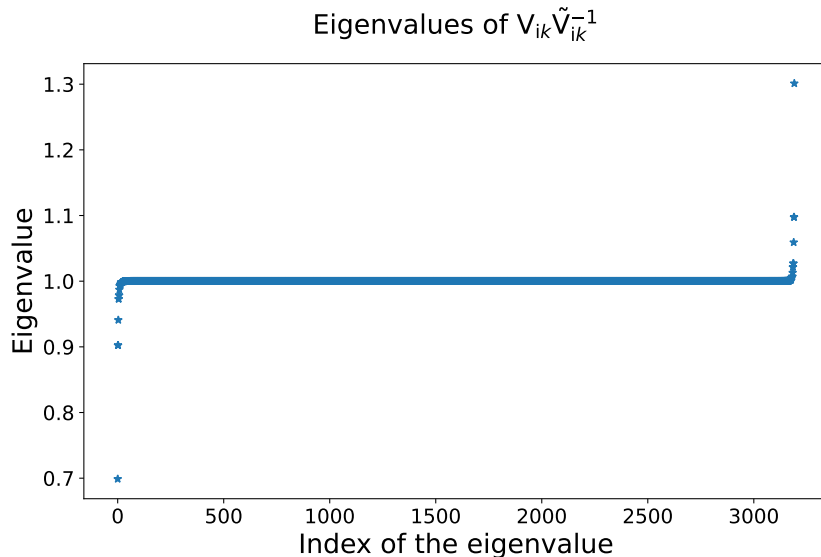


Figure 2: The eigenvalues of the matrix $\mathbf{V}_{ik}\tilde{\mathbf{V}}_{ik}^{-1}$ when $ik = 0.8i$. The scatterers are two spheres with equal radii $r_1 = r_2 = 1$ and the minimal distance between them is $Z = 0.5$. The grid size of the mesh is $h = 0.1$.

4.1. Method I: Inverse-free Krylov subspace method

Consider the eigenvalue problem:

$$\mathbf{V}_{ik}\tilde{\mathbf{V}}_{ik}^{-1}\mathbf{x} = \lambda\mathbf{x}, \quad (9)$$

where λ is the eigenvalue and \mathbf{x} is the corresponding eigenvalue. This eigenvalue problem is equivalent to the following generalized eigenvalue problem:

$$\mathbf{V}_{ik}\tilde{\mathbf{x}} = \lambda\tilde{\mathbf{V}}_{ik}\tilde{\mathbf{x}}. \quad (10)$$

Thus, we can focus on solving the problem (10) instead of (9) to avoid computing the matrix inversion. By [38][39], the authors proposed an inverse-free Krylov subspace method for computing a few extreme eigenvalues of the symmetric definite generalized eigenvalue problem and the following algorithm summarizes this method.

Algorithm 1: Inverse-free Krylov subspace method for computing multiple extreme eigenvalues of the generalized eigenvalue problem $A\mathbf{x} = \lambda B\mathbf{x}$

Input: Symmetric matrix $A \in \mathbb{R}^{n \times n}$, s.p.d matrix $B \in \mathbb{R}^{n \times n}$, an initial approximation \mathbf{x} with $\|\mathbf{x}\| = 1$, the shift $\rho = 1$ and the dimension of the Krylov subspace $m \geq 1$

Output: The approximated extreme eigenvalues of $A\mathbf{x} = \lambda B\mathbf{x}$

- 1: Construct a basis Z_m for the Krylov subspace $K_m = \text{span}(\mathbf{x}, (A - \rho B)\mathbf{x}, \dots, (A - \rho B)^{m-1}\mathbf{x})$ with dimension m
 - 2: Project A and B on Z : $A_m = Z_m^T(A - \rho B)Z_m$, $B_m = Z_m^T B Z_m$
 - 3: Compute all the eigenpairs $\{(\lambda_i, \mathbf{x}_i)\}_{i=1,\dots,m}$ for the matrix pencil (A_m, B_m)
 - 4: Add each eigenvalue in $\{\lambda_i\}_{i=1,\dots,m}$ with the shift $\rho = 1$: $\tilde{\lambda}_i = \lambda_i + 1$, for $i = 1, \dots, m$
-

Algorithm 1 can make us approximate m extreme eigenvalues for the matrix pencil (A, B) where m is the dimension of the Krylov subspace K_m in Step 1, Algorithm 1. Moreover, since most of the eigenvalues of $\mathbf{V}_{ik}\tilde{\mathbf{V}}_{ik}^{-1}$ are around 1, it is better to set the shift ρ as 1, otherwise, we need more iterations to make the eigenvalues approximate to the exact ones [38].

Therefore, for each quadrature point ik_j , for $j = 1, \dots, N$, we can apply Algorithm 1 to compute the eigenvalues $\{\lambda_i^{(j)}\}_{i=1,\dots,m}$ for $\mathbf{V}_{ik_j}\tilde{\mathbf{V}}_{ik_j}^{-1}$, then the value of $\log \det(\mathbf{V}_{ik_j}\tilde{\mathbf{V}}_{ik_j}^{-1})$ can be approximated by

$$\log \det(\mathbf{V}_{ik_j}\tilde{\mathbf{V}}_{ik_j}^{-1}) \approx \sum_{i=1}^m \log(\lambda_i^{(j)}), \quad j = 1, \dots, N.$$

In order to make this inverse-free method become more efficient, one can recycle the subspace obtained from the first wavenumber ik_1 case by extracting several eigenvectors associated with the extremal eigenvalues in Step 3, Algorithm 1 and recovering the eigenvectors for the matrix pair $(\mathbf{V}_{ik_1}, \tilde{\mathbf{V}}_{ik_1})$ by multiplying the basis Z_m in Step 1, Algorithm 1 with the extracted eigenvectors. After orthogonalizing the resulting vectors, they are recycled as a temporary basis for the next wavenumber's case.

For the second wavenumber, we initially compute the approximated eigenvalues ($\{\tilde{\lambda}_i\}$) and eigenvectors ($\{\tilde{\mathbf{x}}_i\}$) with the recycled subspace and use the residual vectors $(\{\mathbf{r}_i\}, \text{ where } \mathbf{r}_i = \mathbf{V}_{ik_2}\tilde{\mathbf{x}}_2 - \tilde{\lambda}_i\tilde{\mathbf{V}}_{ik_1}\tilde{\mathbf{x}}_i)$ to expand the temporary basis. With the expanded subspace, we recompute the eigenpairs for the second wavenumber's case and extract the resulting eigenvectors for the third wavenumber and so on. This modified inverse-free Krylov subspace method based on the recycled subspace is completely described in Algorithm 2.

Algorithm 2: Inverse-free recycled Krylov subspace method for sequences of generalized eigenvalue problems $A^{(i)}\mathbf{x} = \lambda B^{(i)}\mathbf{x}$

Input: N : the number of matrix pencils $(A^{(i)}, B^{(i)})$, an initial approximation \mathbf{x} with $\|\mathbf{x}\| = 1$, the shift $\rho = 1$, the dimension of Krylov subspace $m \geq 1$ and the number of chosen extreme eigenvalues $\{s_i\}_i$, for $i = 1, 2, \dots, (N - 1)$

Output: The approximated extreme eigenvalues of $A\mathbf{x} = \lambda B\mathbf{x}$

1: When $i = 1$:

(a) Compute the basis $Z_m^{(1)}$ for the Krylov subspace

$$K_m^{(1)} = \text{span}(\mathbf{x}, (A^{(1)} - \rho B^{(1)})\mathbf{x}, \dots, (A^{(1)} - \rho B^{(1)})^{m-1}\mathbf{x}) \text{ with dimension } m$$

(b) Project $A^{(1)}$ and $B^{(1)}$ on $Z_m^{(1)}$: $A_m^{(1)} = Z_m^{(1)H}(A^{(1)} - \rho B^{(1)})Z_m^{(1)}$, $B_m^{(1)} = Z_m^{(1)H}B^{(1)}Z_m^{(1)}$

(c) Compute the eigenvalues $\boldsymbol{\lambda}^{(1)} = \{\lambda_1^{(1)}, \dots, \lambda_m^{(1)}\}$ and eigenvectors $\mathbf{X}_m^{(1)} = [\mathbf{x}_1^{(1)}, \dots, \mathbf{x}_m^{(1)}]$ for $A_m^{(1)}\mathbf{x} = \lambda B_m^{(1)}\mathbf{x}$ and note that the approximated eigenvalues for $A^{(1)}\mathbf{x} = \lambda B^{(1)}\mathbf{x}$ are $\{\lambda_1^{(1)} + \rho, \dots, \lambda_m^{(1)} + \rho\}$

(d) Extract s_1 eigenvectors from $\mathbf{X}_m^{(1)}$, which correspond to s_1 extreme eigenvalues and relabel them as $\mathbf{X}_{s_1}^{(1)} = [\mathbf{x}_1^{(1)}, \dots, \mathbf{x}_{s_1}^{(1)}]$

(e) Recover the eigenvectors for $A^{(1)}\mathbf{x} = \lambda B^{(1)}\mathbf{x}$ by computing $Z_m^{(1)}\mathbf{X}_{s_1}^{(1)}$ and orthogonalize it to obtain the temporary basis $\tilde{Z}_{s_1}^{(2)} = \text{orth}(Z_m^{(1)}\mathbf{X}_{s_1}^{(1)})$ for the second matrix pencil $(A^{(2)}, B^{(2)})$

2: When $i = 2$:

(a) Project $A^{(2)}$ and $B^{(2)}$ on $\tilde{Z}_{s_1}^{(2)}$: $\tilde{A}_{s_1}^{(2)} = \tilde{Z}_{s_1}^{(2)H}A^{(2)}\tilde{Z}_{s_1}^{(2)}$, $\tilde{B}_{s_1}^{(2)} = \tilde{Z}_{s_1}^{(2)H}B^{(2)}\tilde{Z}_{s_1}^{(2)}$

(b) Compute the eigenvalues $\tilde{\boldsymbol{\lambda}}^{(2)} = \{\tilde{\lambda}_1^{(2)}, \dots, \tilde{\lambda}_{s_1}^{(2)}\}$ and eigenvectors $\tilde{\mathbf{X}}_{s_1}^{(2)} = [\tilde{\mathbf{x}}_1^{(2)}, \dots, \tilde{\mathbf{x}}_{s_1}^{(2)}]$ for $\tilde{A}_{s_1}^{(2)}\mathbf{x} = \lambda \tilde{B}_{s_1}^{(1)}\mathbf{x}$

(c) Compute the residuals $\mathbf{r}_i^{(2)} = A^{(2)}\tilde{Z}_{s_1}^{(2)}\tilde{\mathbf{x}}_i^{(2)} - \tilde{\lambda}_i^{(2)}B^{(2)}\tilde{Z}_{s_1}^{(2)}\tilde{\mathbf{x}}_i^{(2)}$ for $i = 1, 2, \dots, s_1$ and denote $\mathbf{r}^{(2)} = [\mathbf{r}_1^{(2)}, \dots, \mathbf{r}_{s_1}^{(2)}]$

(d) Construct the basis $Z_{2s_1}^{(2)}$ for $(A^{(2)}, B^{(2)})$ by extending the temporary basis $\tilde{Z}_{s_1}^{(2)}$ with the residues $\mathbf{r}^{(2)}$ and orthogonalizing the extended subspace: $Z_{2s_1}^{(2)} = [\tilde{Z}_{s_1}^{(2)}, \tilde{\mathbf{r}}^{(2)}]$, where $\tilde{\mathbf{r}}^{(2)} = \text{orth}(\mathbf{r}^{(2)})$

(e) Project $A^{(2)}$ and $B^{(2)}$ on $Z_{2s_1}^{(2)}$:

$$A_{2s_1}^{(2)} = Z_{2s_1}^{(2)H}A^{(2)}Z_{2s_1}^{(2)} = \begin{bmatrix} \tilde{A}_{s_1}^{(2)} & \tilde{Z}_{s_1}^{(2)H}A^{(2)}\tilde{\mathbf{r}}^{(2)} \\ \tilde{\mathbf{r}}^{(2)H}A^{(2)}\tilde{Z}_{s_1}^{(2)} & \tilde{\mathbf{r}}^{(2)H}A^{(2)}\tilde{\mathbf{r}}^{(2)} \end{bmatrix},$$

$$B_{2s_1}^{(2)} = Z_{2s_1}^{(2)H}B^{(2)}Z_{2s_1}^{(2)} = \begin{bmatrix} \tilde{B}_{s_1}^{(2)} & \tilde{Z}_{s_1}^{(2)H}B^{(2)}\tilde{\mathbf{r}}^{(2)} \\ \tilde{\mathbf{r}}^{(2)H}B^{(2)}\tilde{Z}_{s_1}^{(2)} & \tilde{\mathbf{r}}^{(2)H}B^{(2)}\tilde{\mathbf{r}}^{(2)} \end{bmatrix}$$

(f) Repeat Step 1(c)-(e) for these projected matrices to compute the approximated eigenvalues $\boldsymbol{\lambda}^{(2)} = \{\lambda_1^{(2)}, \dots, \lambda_{2s_1}^{(2)}\}$ and eigenvectors $\mathbf{X}_{2s_1}^{(2)} = [\mathbf{x}_1^{(2)}, \dots, \mathbf{x}_{2s_1}^{(2)}]$ for $(A_{2s_1}^{(2)}, B_{2s_1}^{(2)})$ and obtain the temporary basis $\tilde{Z}_{s_2}^{(3)}$ for the third matrix pencil $(A^{(3)}, B^{(3)})$

3: For $i = 3, \dots, N$, repeat the Step 2 to compute the approximated eigenvalues $\boldsymbol{\lambda}^{(i)} = \{\lambda_1^{(i)}, \dots, \lambda_{2s_{i-1}}^{(i)}\}$ and eigenvectors $\mathbf{X}_{2s_{i-1}}^{(i)} = [\mathbf{x}_1^{(i)}, \dots, \mathbf{x}_{2s_{i-1}}^{(i)}]$ for each matrix pencil

In this case, the value of $\log \det(\mathbf{V}_{ik_j} \tilde{\mathbf{V}}_{ik_j}^{-1})$ can be approximated by

$$\log \det(\mathbf{V}_{ik_j} \tilde{\mathbf{V}}_{ik_j}^{-1}) \approx \begin{cases} \sum_{i=1}^m \log(\lambda_i^{(j)}) & j = 1 \\ \sum_{i=1}^{2s_{j-1}} \log(\lambda_i^{(j)}) & j = 2, \dots, N \end{cases} \quad (11)$$

4.2. Method II: Standard Arnoldi method

Another efficient approach for computing $\log \det(\mathbf{V}_{ik} \tilde{\mathbf{V}}_{ik}^{-1})$ is to initially construct the Krylov subspace $K_m(\mathbf{V}_{ik} \tilde{\mathbf{V}}_{ik}^{-1}, \mathbf{b})$, where \mathbf{b} is some initial vector and m is the dimension of this Krylov subspace. Afterwards, we implement the standard Arnoldi iteration to obtain the orthogonal basis of this order- m Krylov subspace and project the matrix $\mathbf{V}_{ik} \tilde{\mathbf{V}}_{ik}^{-1}$ onto this basis. This projection matrix is called the Hessenberg matrix and we denote it as H_m . By [40], the eigenvalues of H_m (which are also called Ritz eigenvalues) can give good approximations on extreme eigenvalues of $\mathbf{V}_{ik} \tilde{\mathbf{V}}_{ik}^{-1}$. The following algorithm lists the general steps described above.

Algorithm 3: Standard Arnoldi method for computing multiple extreme eigenvalues of the eigenvalue problem $AB^{-1}\mathbf{x} = \mu\mathbf{x}$

Input: Block matrix $A \in \mathbb{R}^{n \times n}$, diagonal block matrix $B \in \mathbb{R}^{n \times n}$ and the dimension of the Krylov subspace $m \geq 1$

Output: The approximated extreme eigenvalue of $AB^{-1}\mathbf{x} = \mu\mathbf{x}$

- 1: Use standard Arnoldi method to compute the Hessenberg matrix H_m of AB^{-1}
 - 2: Compute all the eigenpairs $\{(\mu_i, \mathbf{x}_i)\}_{i=1,\dots,m}$ of H_m
-

Remark 3. During the Arnoldi iteration process, one needs to multiply the inverse matrix $\tilde{\mathbf{V}}_{ik}^{-1}$ with some

vector $\mathbf{v} = \begin{bmatrix} \mathbf{v}_1 \\ \vdots \\ \mathbf{v}_N \end{bmatrix}$. In order to avoid directly computing the matrix inversion, one can firstly compute LU decomposition for each diagonal block matrix $\mathbf{V}_{ii}(ik) = \mathbf{L}_{ii}\mathbf{U}_{ii}$, for $i = 1, 2, \dots, N$, where \mathbf{L}_{ii} and \mathbf{U}_{ii} are lower and upper triangular matrices, respectively and solve the linear system $\mathbf{L}_{ii}\mathbf{U}_{ii}\mathbf{x}_i = \mathbf{v}_i$ for $i = 1, 2, \dots, N$. Finally,

the resulting vector is $\mathbf{x} = \begin{bmatrix} \mathbf{x}_1 \\ \vdots \\ \mathbf{x}_1 \end{bmatrix}$.

By denoting the the eigenvalues of H_m as $\{\mu_i\}_{i=1,\dots,m}$, the value of $\log \det(\mathbf{V}_{ik} \tilde{\mathbf{V}}_{ik}^{-1})$ can be approximated by

$$\log \det(\mathbf{V}_{ik} \tilde{\mathbf{V}}_{ik}^{-1}) \approx \sum_{i=1}^m \log(\mu_i).$$

Same with the inverse-free Krylov subspace method, one can also recycle the eigenvectors associated with the extreme eigenvalues from the initial subspace for the first wavenumber, expand it with some vectos (In Algorithm 2, they are residual vectors) and use the complemented basis for the second wavenumber's case. Algorithm 4 summarizes the whole steps for this recycling process.

Algorithm 4: Standard Arnoldi methods with recycled subspaces for sequences of eigenvalue problems

$$A^{(i)} (B^{(i)})^{-1} \mathbf{x} = \mu \mathbf{x}$$

Input: N : the number of matrices $A^{(i)} (B^{(i)})^{-1}$, where $A^{(i)}$ are block matrices and $B^{(i)}$ are diagonal block matrices, an initial approximation \mathbf{x} with $\|\mathbf{x}\| = 1$, the shift $\rho = 1$, the dimension of Krylov subspace $m \geq 1$ and the number of chosen extreme eigenvalues $\{s_i\}_i$, for $i = 1, 2, \dots, (N - 1)$

1: When $i = 1$:

- (a) Apply the standard Arnoldi method to compute the Arnoldi vectors $Z_m^{(1)}$ and Hessenberg matrix $H_m^{(1)}$ for $A^{(1)} (B^{(1)})^{-1}$, which satisfies $H_m^{(1)} = Z_m^{(1)H} (A^{(1)} (B^{(1)})^{-1}) Z_m^{(1)}$
- (b) Compute the eigenvalues $\boldsymbol{\mu}^{(1)} = \{\mu_1^{(1)}, \dots, \mu_m^{(1)}\}$ and eigenvectors $\mathbf{X}_m^{(1)} = [\mathbf{x}_1^{(1)}, \dots, \mathbf{r}_m^{(1)}]$ for $H_m^{(1)}$
- (c) Extract s_1 eigenvectors from $\mathbf{X}_m^{(1)}$, which correspond to s_1 extreme eigenvalues and relabel them as $\mathbf{X}_{s_1}^{(1)} = [\mathbf{x}_1^{(1)}, \dots, \mathbf{x}_{s_1}^{(1)}]$
- (d) Recover the eigenvectors for $A^{(1)} (B^{(1)})^{-1} \mathbf{x} = \mu \mathbf{x}$ by computing $Z_m^{(1)} \mathbf{X}_{s_1}^{(1)}$ and orthogonalize it to obtain the temporary basis $\tilde{Z}_{s_1}^{(2)} = \text{orth}(Z_m^{(1)} \mathbf{X}_{s_1}^{(1)})$ for the second eigenvalue problem $A^{(2)} (B^{(2)})^{-1} \mathbf{x} = \lambda \mathbf{x}$

2: When $i = 2$:

- (a) Project $A^{(2)} (B^{(2)})^{-1}$ on $\tilde{Z}_{s_1}^{(2)}$:

$$\tilde{H}_{s_1}^{(2)} = \tilde{Z}_{s_1}^{(2)H} (A^{(2)} (B^{(2)})^{-1}) \tilde{Z}_{s_1}^{(2)}$$

- (b) Compute the eigenvalues $\tilde{\boldsymbol{\mu}}^{(2)} = \{\tilde{\mu}_1^{(2)}, \dots, \tilde{\mu}_{s_1}^{(2)}\}$ and eigenvectors $\tilde{\mathbf{X}}_{s_1}^{(2)} = [\tilde{\mathbf{x}}_1^{(2)}, \dots, \tilde{\mathbf{x}}_{s_1}^{(2)}]$ for $A^{(2)} (B^{(2)})^{-1} \mathbf{x} = \lambda \mathbf{x}$
- (c) Compute the residuals $\mathbf{r}_i^{(2)} = (A^{(2)} (B^{(2)})^{-1}) \tilde{Z}_{s_1}^{(2)} \tilde{\mathbf{x}}_i^{(2)} - \tilde{\mu}_i^{(2)} \tilde{Z}_{s_1}^{(2)} \tilde{\mathbf{x}}_i^{(2)}$, for $i = 1, 2, \dots, s_1$ and denote $\mathbf{r}^{(2)} = [\mathbf{r}_1^{(2)}, \dots, \mathbf{r}_{s_1}^{(2)}]$
- (d) Construct the basis $Z_{2s_1}^{(2)}$ for $A^{(2)} (B^{(2)})^{-1}$ by extending the temporary basis $\tilde{Z}_{s_1}^{(2)}$ with the residues $\mathbf{r}^{(2)}$ and orthogonalizing the extended subspace: $Z_{2s_1}^{(2)} = [\tilde{Z}_{s_1}^{(2)}, \tilde{\mathbf{r}}^{(2)}]$, where $\tilde{\mathbf{r}}^{(2)} = \text{orth}(\mathbf{r}^{(2)})$
- (e) Project $A^{(2)} (B^{(2)})^{-1}$ on $Z_{2s_1}^{(2)}$:

$$H_{2s_1}^{(2)} = Z_{2s_1}^{(2)H} (A^{(2)} (B^{(2)})^{-1}) Z_{2s_1}^{(2)} = \begin{bmatrix} \tilde{H}_{s_1}^{(2)} & \tilde{Z}_{s_1}^{(2)H} (A^{(2)} (B^{(2)})^{-1}) \tilde{\mathbf{r}}^{(2)} \\ \tilde{\mathbf{r}}^{(2)H} (A^{(2)} (B^{(2)})^{-1}) \tilde{Z}_{s_1}^{(2)} & \tilde{\mathbf{r}}^{(2)H} (A^{(2)} (B^{(2)})^{-1}) \tilde{\mathbf{r}}^{(2)} \end{bmatrix}$$

- (f) Repeat Step 1(c)-(e) for the projected matrix $H_{2s_1}^{(2)}$ to compute the approximated eigenvalues $\boldsymbol{\mu}^{(2)} = \{\mu_1^{(2)}, \dots, \mu_{2s_1}^{(2)}\}$ and eigenvectors $\mathbf{X}_{2s_1}^{(2)} = [\mathbf{x}_1^{(2)}, \dots, \mathbf{x}_{2s_1}^{(2)}]$ and obtain the temporary basis $\tilde{Z}_{s_2}^{(3)}$ for the third eigenvalue problem $A^{(3)} (B^{(3)})^{-1} \mathbf{x} = \lambda \mathbf{x}$

- 3: For $i = 3, \dots, N$, repeat the Step 2 to compute the approximated eigenvalues $\boldsymbol{\mu}^{(i)} = \{\mu_1^{(i)}, \dots, \mu_{2s_{i-1}}^{(i)}\}$ and eigenvectors $\mathbf{X}_{2s_{i-1}}^{(1)} = [\mathbf{x}_1^{(i)}, \dots, \mathbf{x}_{2s_{i-1}}^{(i)}]$ for each eigenvalue problem
-

With Algorithm 4, the value of $\log \det(V_{ik_j} \tilde{V}_{ik_j}^{-1})$ can be approximated by

$$\log \det(\mathbf{V}_{ik_j} \tilde{\mathbf{V}}_{ik_j}^{-1}) \approx \begin{cases} \sum_{i=1}^m \log(\mu_i^{(j)}) & j = 1 \\ \sum_{i=1}^{2s_{j-1}} \log(\mu_i^{(j)}) & j = 2, \dots, N \end{cases} \quad (12)$$

4.3. Comparison between inverse-free Krylov subspace and standard Arnoldi method with or without recycling subspaces

In this part, the performances on approximating the $\log \det \mathbf{V}_{ik} \tilde{\mathbf{V}}_{ik}^{-1}$ and the complexity of Algorithm 1-4 will be compared. Consider two spheres with equal radii $r_1 = r_2 = 1$ and the minimal distance between them is denoted as Z , which is set as 0.5, 1.5 and 3.0. The dimension of the Krylov subspace m in Algorithm 1, Algorithm 2, Step 1 of Algorithm 2, Algorithm 3 and Step 1 of Algorithm 4 is $m = 100$. The rule for extracting the eigenvectors in recycled scheme is that only the eigenvector associated with the extreme eigenvalue whose logarithm value is greater than 10^{-5} would be recycled.

Table 1 lists the relative error for approximating the value of $\log \det \mathbf{V}_{ik} \tilde{\mathbf{V}}_{ik}^{-1}$ computed via the inverse-free Krylov subspace method and standard Arnoldi method with or without recycling the subspace. It indicates that for with the settings above, one can have at least three significant digits accuracy.

Distance Z	Quadrature points k	Inverse-free (no recycling)	Inverse-free (recycling)	Standard Arnoldi (no recycling)	Standard Arnoldi (recycling)
$Z = 0.5$	0	9.79×10^{-4}	9.79×10^{-4}	9.29×10^{-4}	9.29×10^{-4}
	0.0540	9.67×10^{-4}	9.78×10^{-5}	4.91×10^{-5}	1.37×10^{-6}
	0.111	1.22×10^{-3}	2.79×10^{-5}	5.29×10^{-5}	5.17×10^{-6}
	0.171	1.15×10^{-3}	2.42×10^{-5}	2.78×10^{-5}	8.45×10^{-5}
	0.236	1.25×10^{-3}	9.10×10^{-6}	1.12×10^{-4}	2.76×10^{-5}
$Z = 1.5$	0	9.48×10^{-4}	9.54×10^{-4}	3.41×10^{-7}	3.41×10^{-7}
	0.0540	1.02×10^{-3}	2.87×10^{-4}	5.89×10^{-7}	3.97×10^{-8}
	0.111	1.16×10^{-3}	1.80×10^{-4}	1.45×10^{-8}	2.35×10^{-4}
	0.171	1.25×10^{-3}	1.35×10^{-4}	2.70×10^{-6}	1.06×10^{-4}
	0.236	1.33×10^{-3}	4.77×10^{-5}	3.14×10^{-7}	4.87×10^{-5}
$Z = 3.0$	0	1.38×10^{-3}	1.38×10^{-3}	8.55×10^{-12}	8.55×10^{-12}
	0.0540	1.54×10^{-3}	4.34×10^{-4}	3.46×10^{-9}	2.61×10^{-5}
	0.111	1.81×10^{-3}	2.89×10^{-4}	5.02×10^{-10}	5.43×10^{-7}
	0.171	2.13×10^{-3}	2.35×10^{-4}	4.82×10^{-8}	2.50×10^{-5}
	0.236	2.54×10^{-3}	2.13×10^{-4}	5.07×10^{-9}	1.59×10^{-5}

Table 1: Relative error for approximating the value of $\log \det \mathbf{V}_{ik} \tilde{\mathbf{V}}_{ik}^{-1}$ on the first five consecutive quadrature points via the inverse-free Krylov subspace and standard Arnoldi methods with/without subspace recycled. The scatterers are two spheres with equal radii $R = 1$ with distance $Z = 0.5, 1.5$ and 3.0 .

To further compare the efficiency of these methods, we explore the number of matrix-vector multiplications for these methods on computing the Casimir energy and they are listed inside Table 2. In addition, Figure 3 and Figure 4 plot the number of matrix-vector multiplications that we need to compute the Casimir energy between two spheres with distance $Z = 0.5, 1.5$ and 3.0 by using these methods with or without recycling the subspaces. One can notice that the methods with recycling the subspace have similar number of matvec and they also

have smaller number of matvec than the non-recycling methods. Therefore, for all the numerical experiments in Section 5, we would apply the methods with subspaced recycled to compute the Casimir energy.

Inverse-free Krylov subspace method		Standard Arnoldi method	
Without recycling	With recycling	Without recycling	With recycling
$(2m - 1)N$	$(2m - 1) + 2 \sum_{i=1}^{N-1} s_i$	$(m - 1)N$	$(m - 1) + 2 \sum_{i=1}^{N-1} s_i$

Table 2: The number of matrix-vector multiplications inside the inverse-free Krylov subspace and standard Arnoldi methods with or without recycling subspaces. N is the number of wavenumbers, m is the dimension of the Krylov subspace for the first wavenumber (in recycling case); for all the wavenumbers (in non-recycling case), and s_i is the number of the extracted eigenvectors for the i th wavenumber's case (in recycling case).

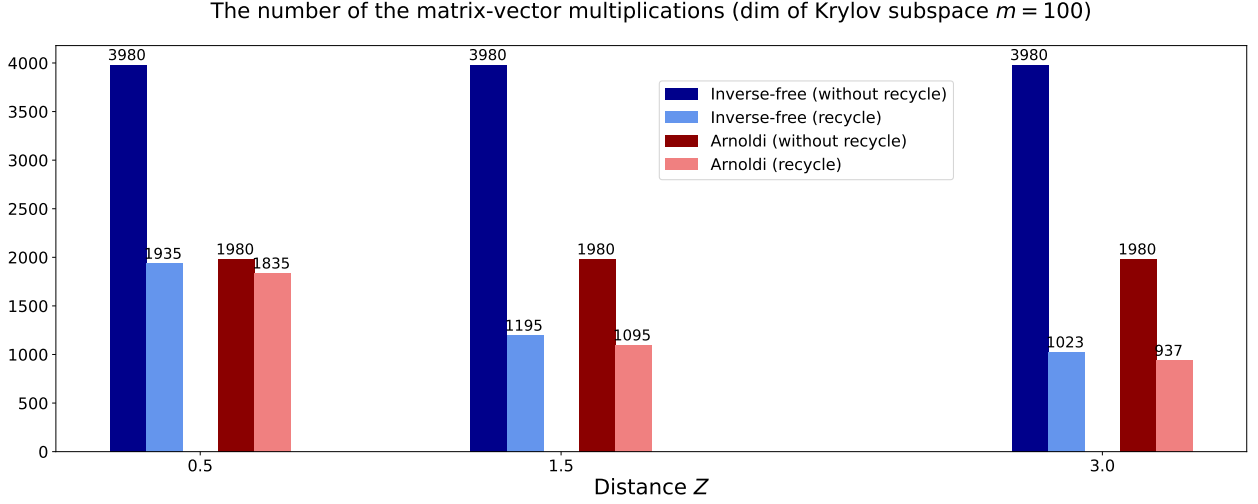


Figure 3: The number of the matrix-vector products inside inverse-free and standard Arnoldi methods with or without recycling subspace. The scatterers are two spheres with equal radii $R = 1$ and distance Z is 0.5, 1.5 and 3.0. The dimension of the Krylov subspace is set as $m = 100$.

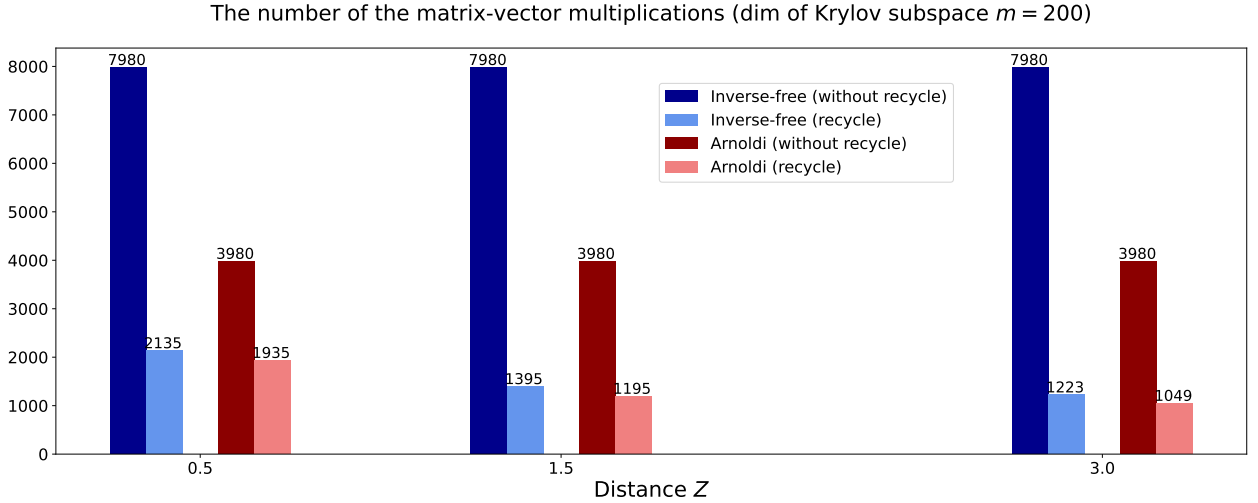


Figure 4: The number of the matrix-vector products inside inverse-free and standard Arnoldi methods with or without recycling subspace. The scatterers are two spheres with equal radii $R = 1$ and distance Z is 0.5, 1.5 and 3.0. The dimension of the Krylov subspace is set as $m = 200$.

5. Numerical experiments

In this section, we are going to show the numerical results for computing the Casimir energy between two perfectly conducting objects, which are spheres, menger sponges, ice crystals and ellipsoids. The reference value of the Casimir energy is computed by the Richardson extrapolation method which is often used for obtaining the higher-order estimate at zero grid spacing. Denote $\mathcal{E}_{\text{fine}}$ and $\mathcal{E}_{\text{coarse}}$ as the Casimir energy numerically computed from the formula (5) by setting the grid size h as h_{fine} and h_{coarse} ($h_{\text{fine}} < h_{\text{coarse}}$), separately. Then, the high-accuracy result $\mathcal{E}_{\text{extrapolation}}$ can be generated from the following formula:

$$\mathcal{E}_{\text{extrapolation}} \approx \frac{h_{\text{coarse}}^2 \mathcal{E}_{\text{fine}} - h_{\text{fine}}^2 \mathcal{E}_{\text{coarse}}}{h_{\text{coarse}}^2 - h_{\text{fine}}^2}. \quad (13)$$

In addition, the asymptotic series of the Casimir energy with large separation between scatterers are also available in two spheres' case and the series can be found in [24] for both equal and unequal radii's cases.

5.1. Two spheres case

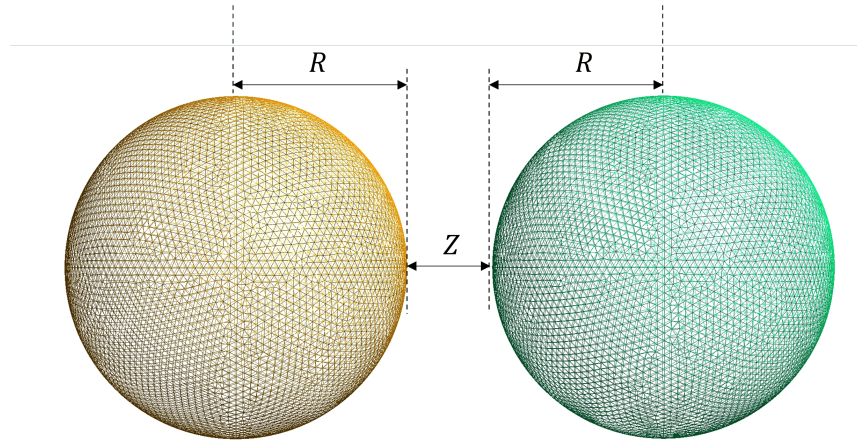


Figure 5: Two spheres with equal radii: $R = 1$ represents the radius of the spheres and Z is the distance between them. $h_{\text{coarse}} = 0.1$: $\dim(V_{ik}) = 3192$, N^{Ω} of elements on both grids = 6384; $h_{\text{fine}} = 0.05$: $\dim(V_{ik}) = 12603$, N^{Ω} of elements on both grids = 25180

Consider two perfectly conducting spheres with equal radii R in Figure 5. By denoting the distance between them as Z , the asymptotic expression of the integrand of the Casimir integral formula (5) introduced in [32] is written as:

$$\Xi(k) = -\frac{R_1 R_2}{4Z(R_1 + R_2 + Z)} e^{2iZk} + o(e^{-2Z\text{Im}k}), \quad (14)$$

where R_1 and R_2 are the radius of the spheres.

Figure 6 plots the quotient of the leading term in (14) and the estimated integrand value on different wavenumbers ik . This quotient provides with a good estimate on the upperbound of the integration of the Casimir energy formula (5). For example, when the distance $Z = 1.5$, if k in wavenumber ik is larger than 7, the quotient gets far away from 1, which means the approximated integrand value is not close to the asymptotic term and 7i is chosen as the upperbound when $Z = 1.5$. The following table lists the upperbound of the integration for the distance Z varying from 0.5 to 3.0.

Distance Z	0.5	0.75	1.0	1.25	1.5	1.75	2.0	2.25	2.5	2.75	3.0
Upperbound	24i	17i	13i	9i	7i	6i	6i	5i	5i	4i	4i

Table 3: The estimated upperbound for the Casimir energy formula for different minimal distance Z varying from 0.5 to 3.0.

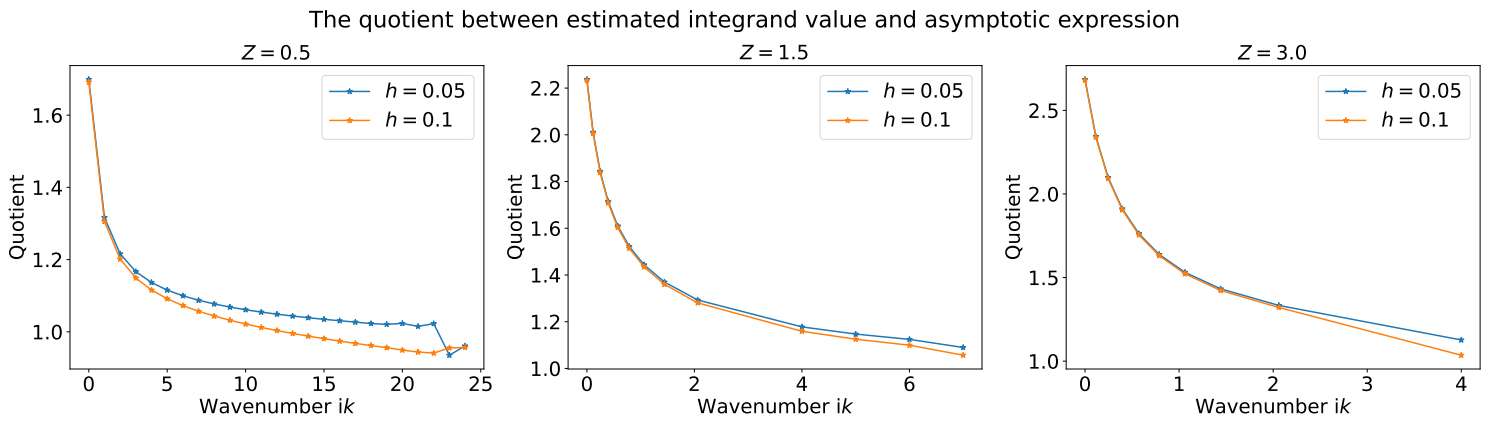


Figure 6: The quotient of the leading term of the series (14) and the estimated integrand value along the imaginary axis with grid size h set as $h_{\text{coarse}} = 0.1$ and $h_{\text{fine}} = 0.05$ in two spheres with equal radii's case. The radius of the spheres is $R = 1$ and the minimal distance between them is $Z = 0.5, 1.5$ and 3.0 .

Remark 4 (Determine the upperbound of the integration from the error tolerance). *By Figure 1, since the integrand value $\log \det V_{ik} \tilde{V}_{ik}^{-1}$ shares the same trend with e^{-2Zk} in (5), one can apply the function $f(k) = Ce^{-2Zk}$ to fit the curve of the estimated integrand values. With the coefficient C determined, one can estimate the absolute error for approximating the Casimir integral by computing:*

$$\epsilon \approx \int_{\kappa}^{\infty} f(k) dk = \frac{Ce^{-2Z\kappa}}{2Z},$$

where κ is the upperbound of the integration. Meanwhile, one can also determine the upperbound of the integration with regard to different error tolerance.

For example, if one aims to have at least three significant digits of the exact value of the Casimir integral, the upperbound can be set as the following table lists:

Distance Z	0.5	0.75	1.0	1.25	1.5	1.75	2.0	2.25	2.5	2.75	3.0
Upperbound	10i	7i	5i	5i	4i	3i	3i	2i	2i	2i	2i

Table 4: The estimated upperbound for the Casimir energy formula for different minimal distance Z varying from 0.5 to 3.0.

With the upperbound of the integration determined, one can start to estimate the Casimir energy between two spheres with radius $R = 1$ at the distance of Z via the formula (5) in two different refinement levels: $h_{\text{fine}} = 0.05$ ($\dim(V_{ik}) = 12603$) and $h_{\text{coarse}} = 0.1$ ($\dim(V_{ik}) = 3192$).

Afterwards, the extrapolation result can be obtained by substituting these Casimir energy estimates into the formula (13). This result would be regarded as the extrapolation value of the Casimir energy, which would be used to compare with the estimates derived from the asymptotic series introduced below.

According to [24], the Casimir energy between two spheres (with equal radii R) at asymptotically large separations can be obtained as a series in terms of the ratio of centre distance L ($L = 2R + Z$) to sphere radius R :

$$\mathcal{E} = -\frac{\hbar c}{\pi} \frac{1}{L} \sum_{n=0}^{\infty} b_n \left(\frac{R}{L} \right)^{n+2}, \quad (15)$$

where the first six coefficients are $b_0 = -1/4$, $b_1 = -1/4$, $b_2 = -77/48$, $b_3 = -25/16$, $b_4 = -29837/2880$, $b_5 = -6491/1152$. Figure 7 shows the comparison between the Casimir energy computed from asymptotic series (15) and the exact value evaluated through Richardson extrapolation. Here, we observe that the asymptotic value gradually approaches to the exact value as the distance Z increases since the asymptotic expansion (15) only works when the distance between two spheres is asymptotically large.

Two spheres with equal radii

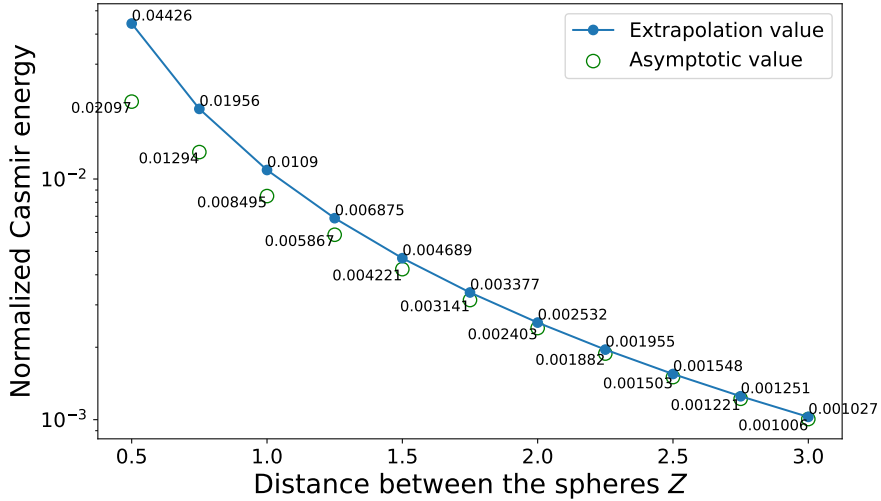


Figure 7: Normalized Casimir energy² in two spheres with equal radii's case. The radius is $R = 1$ and the distance Z ranges from 0.5 to 3.0. The exact value of the (normalized) Casimir energy has been written beside the data point, which is round up to 4 significant digits.

Figure 8 shows the relative distance between the estimated Casimir energy computed through inverse-free Krylov subspace method with subspace recycled (solid blue triangles), standard Arnoldi method with subspace recycled (solid red circles), asymptotic series (solid black squares) and the extrapolation values. For both efficient methods introduced in Section 4, the dimension of the Krylov subspace is set as $m = 100$. In addition, in the recycling process, only the eigenvectors associated with the extreme eigenvalues whose logarithm is larger than 10^{-5} would be extracted and recycled. With these settings, these two methods with subspace recycled can achieve at least three significant digits accuracy on approximating the Casimir energy.

Two spheres with equal radii

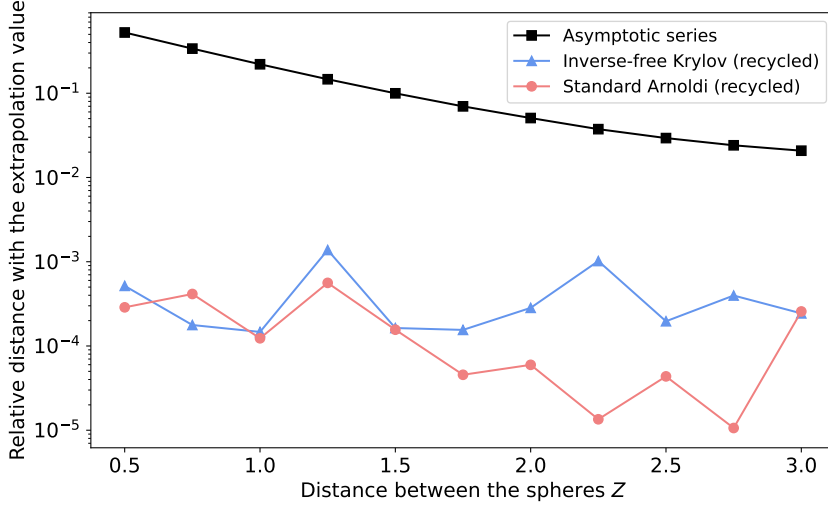


Figure 8: Spheres with equal radii's case: relative distance between the reference value (computed by Richardson extrapolation) with the asymptotic series (solid black square) and the estimates evaluated from the standard Arnoldi method with subspace recycled (solid red circles) and inverse-free Krylov subspace method with subspace recycled (solid blue triangles). The dimension of the Krylov subspace is $m = 100$.

²The normalized Casimir energy is $\mathcal{E}/\hbar c$, for \mathcal{E} defined in (5).

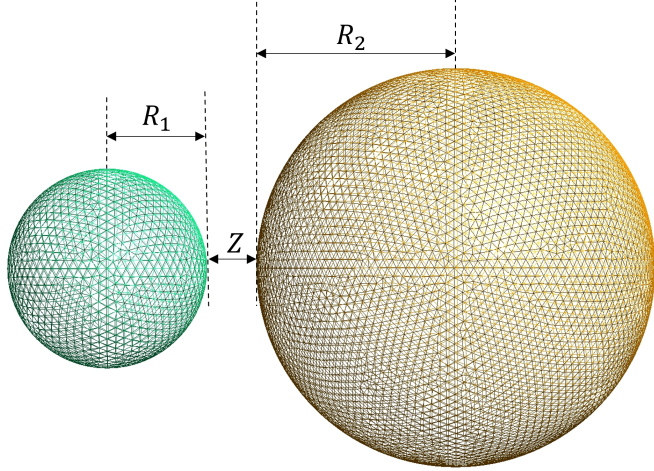


Figure 9: Two spheres with unequal radii: $R_1 = 0.5$ and $R_2 = 1$ represent the radius of the spheres and Z is the distance between them. $h_{\text{coarse}} = 0.1$: $\dim(V_{ik}) = 2023$, N^{Ω} of elements on both grids = 4038; $h_{\text{fine}} = 0.05$: $\dim(V_{ik}) = 7891$, N^{Ω} of elements on both grids = 15774

When the perfectly conducting spheres have different radii R_1 , R_2 (see Figure 9), one can still use the asymptotic expansion (14) to determine the upperbound of the integration in the Casimir energy formula.

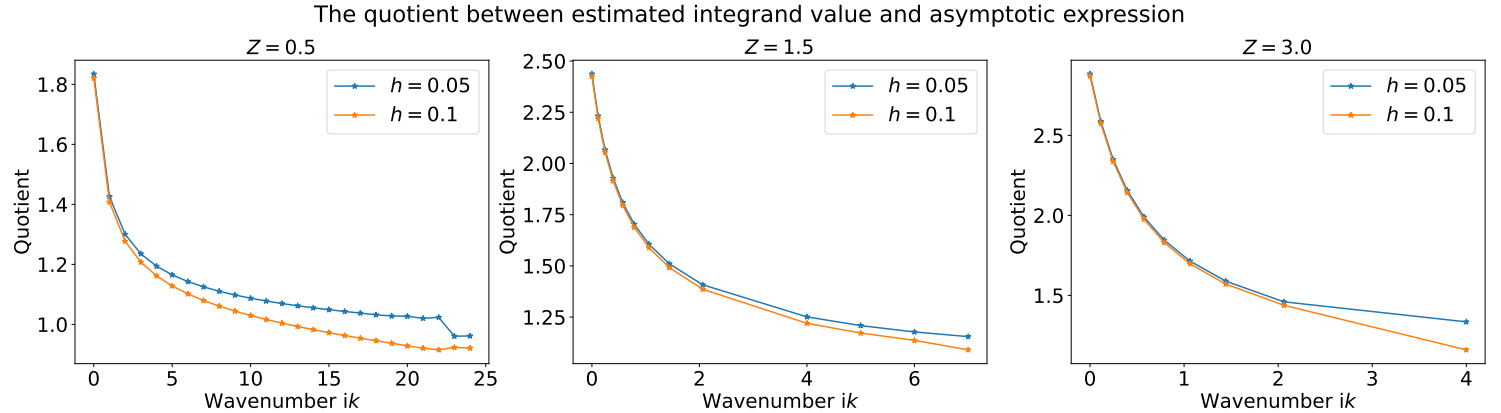


Figure 10: Absolute distance between the approximated integrand value of the Casimir energy formula and the first term in asymptotic expansion (14), and compare this value with the exponential $e^{-2Z\text{Im}k}$. The radii of the spheres are equal to $R_1 = 1$ and $R_2 = 0.5$, and the minimal distance Z between them is 0.5, 1.5 and 3.0. The absolute distance is in solid blue triangles when grid size $h = 0.1$ and in solid orange circles when $h = 0.05$.

Again, with Figure 10, one can easily estimate the upperbound and the results are listed in Table 5.

Distance Z	0.5	0.75	1.0	1.25	1.5	1.75	2.0	2.25	2.5	2.75	3.0
Upperbound	24i	17i	13i	9i	7i	6i	6i	5i	5i	4i	4i

Table 5: The estimated upperbound for the Casimir energy formula for different minimal distance Z varying from 0.5 to 3.0.

By recalling the Remark 4, in order to have at least three significant digits matching with the exact value of the Casimir energy, the upperbound can be set as:

Distance Z	0.5	0.75	1.0	1.25	1.5	1.75	2.0	2.25	2.5	2.75	3.0
Upperbound	10i	6i	6i	4i	4i	3i	3i	3i	3i	3i	3i

Table 6: The estimated upperbound for the Casimir energy formula for different minimal distance Z varying from 0.5 to 3.0.

Afterwards, by denoting the centre distance as $L = R_1 + R_2 + Z$, the asymptotic expansion of the Casimir energy at asymptotically large distance can be written as:

$$\mathcal{E} = -\frac{\hbar c}{\pi} \frac{1}{L} \sum_{n=0}^{\infty} \tilde{b}_n(\eta) \left(\frac{R_1}{L} \right)^{n+2}, \quad (16)$$

where the coefficients $\{\tilde{b}_n\}$ depend on the parameter $\eta = R_2/R_1$ and the first six coefficients are

$$\begin{aligned} \tilde{b}_0 &= -\frac{\eta}{4}, & \tilde{b}_1 &= -\frac{\eta + \eta^2}{8}, & \tilde{b}_2 &= -\frac{34(\eta + \eta^3) + 9\eta^2}{48}, & \tilde{b}_3 &= -\frac{2(\eta + \eta^4) + 23(\eta^2 + \eta^3)}{32}, \\ \tilde{b}_4 &= -\frac{8352(\eta + \eta^5) + 1995(\eta^2 + \eta^4) + 38980\eta^3}{5760}, & \tilde{b}_5 &= -\frac{-1344(\eta + \eta^6) + 5478(\eta^2 + \eta^5) + 2357(\eta^3 + \eta^4)}{2304}. \end{aligned}$$

In the following experiment, the radii of the spheres shown in Figure 9 are set as $R_1 = 0.5$ and $R_2 = 1$. As in the previous example, the exact value of the Casimir energy is computed through the Richardson extrapolation formula (13), where the coarse and fine grid size are $h_{\text{fine}} = 0.05$ ($\dim(V_{ik}) = 7893$) and $h_{\text{coarse}} = 0.1$ ($\dim(V_{ik}) = 2023$), separately.

In this case, the asymptotic value of the Casimir energy was estimated by the series (16) and the comparison between the exact value and asymptotic one is shown in Figure 11. Again, one can notice that when the distance between two spheres decreases, the asymptotic value gets close to the exact one and the reason for this is clearly stated in the above equal radii's case.

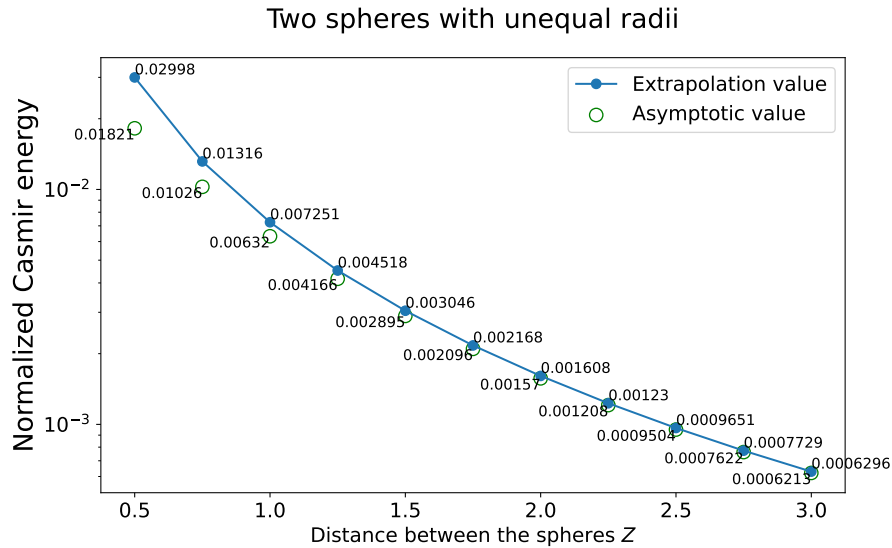


Figure 11: Normalized Casimir energy in two spheres with unequal radii's case. The radius is $R = 1$ and the distance Z ranges from 0.5 to 3.0. The exact value of the (normalized) Casimir energy has been written beside the data point, which is round up to 4 significant digits.

By keeping all the experimental settings being the same with the equal radii's case, the numerical experiments on testing the performance of the inverse-free and standard Arnoldi methods with subspace recycled have been done in the unequal radii's case and the results are shown in Figure 12.

Two spheres with unequal radii

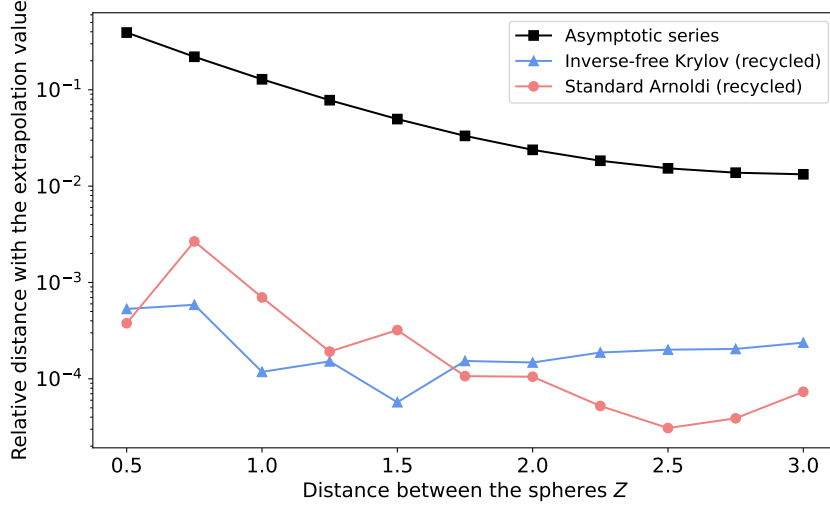


Figure 12: Spheres with unequal radii's case: relative distance between the reference value (computed by Richardson extrapolation) with the asymptotic series (solid black square) and the estimates evaluated from the standard Arnoldi method with subspace recycled (solid red circles) and inverse-free Krylov subspace method with subspace recycled (solid blue triangles). The dimension of the Krylov subspace is $m = 100$.

5.2. Realistic objects case

In this part, the Casimir energy between the objects with special shapes such as the menger sponges, ice crystals and ellipsoids will be computed through the Richardson extrapolation mentioned in the beginning of this section and the values labelled in the following figures are always round up to 4 significant digits.

Figure 13 plots the menger sponges in different levels (0, 1 and 2) and the length of these sponges is always 1. Afterwards, the Casimir energy between two menger sponges in the same level are listed in Table 7. In addition, inside the extrapolation process, when $h_{\text{fine}} = 0.05$, the $\dim(V_{ik}) = 5664, 8510$ and 27136 and when $h_{\text{coarse}} = 0.1$, the $\dim(V_{ik}) = 1456, 3092$ and 14464 in different level (0, 1 and 2) cases, separately. By comparing the data point in this table, it is easy to find that the Casimir energy decreases as the number of the iteration increases since the cross-sectional area gets smaller.

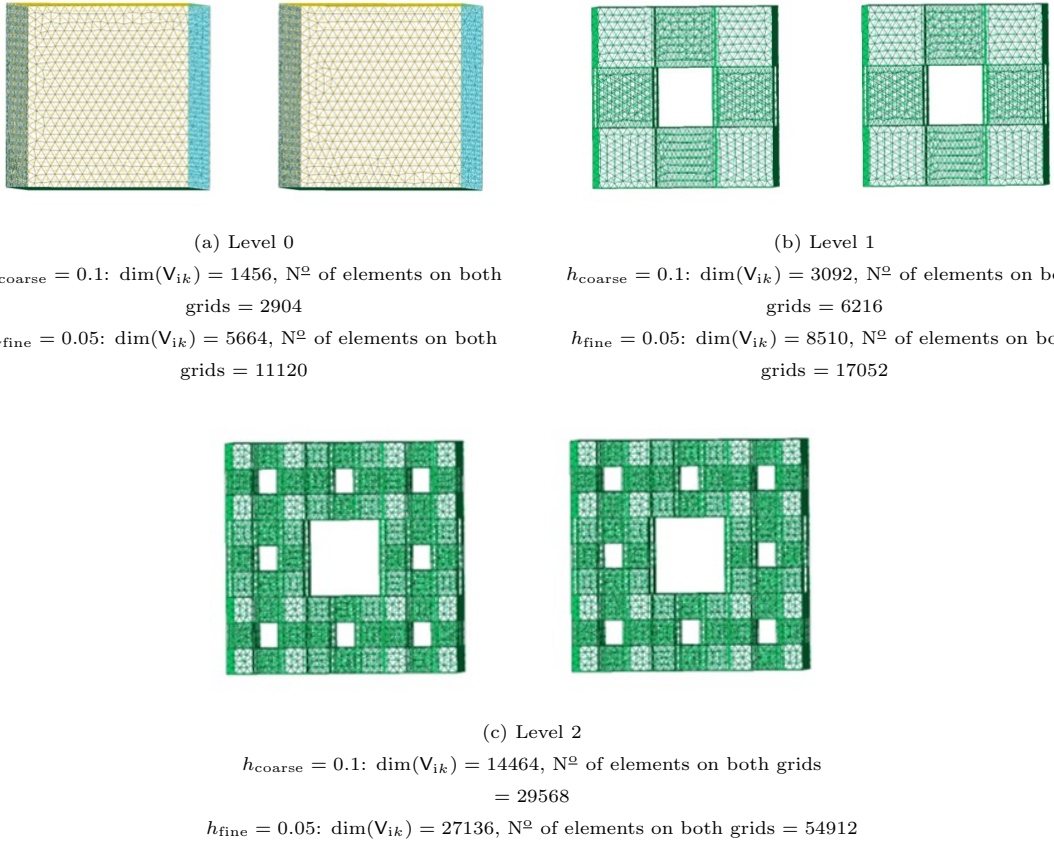


Figure 13: Menger sponges in different levels. The length of each sponge is 1.

Normalized Casimir energy in two menger sponges' case			
Distance	Level 0	Level 1	Level 2
0.5	0.08350	0.08229	0.08112
0.75	0.02737	0.02688	0.02670
1.0	0.01305	0.01288	0.01282
1.25	0.007357	0.007283	0.007252
1.5	0.004607	0.004568	0.004551
1.75	0.003099	0.003076	0.003065
2.0	0.002195	0.002181	0.002174
2.25	0.001618	0.001608	0.001603
2.5	0.001230	0.001223	0.001220
2.75	0.0009593	0.0009541	0.0009514
3.0	0.0007638	0.0007598	0.0007577

Table 7: Normalized Casimir energy in two menger sponges' case

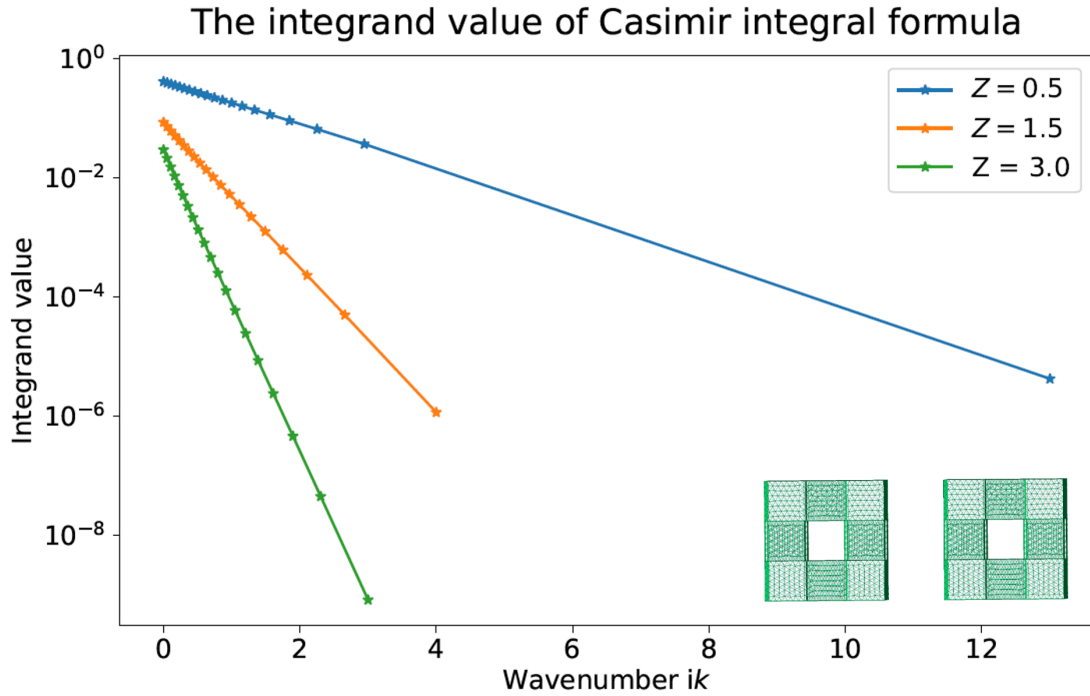


Figure 14: The integrand of the Casimir energy between two menger sponges in Level 1 with distance $Z = 0.5, 1.5$ and 3.0 .

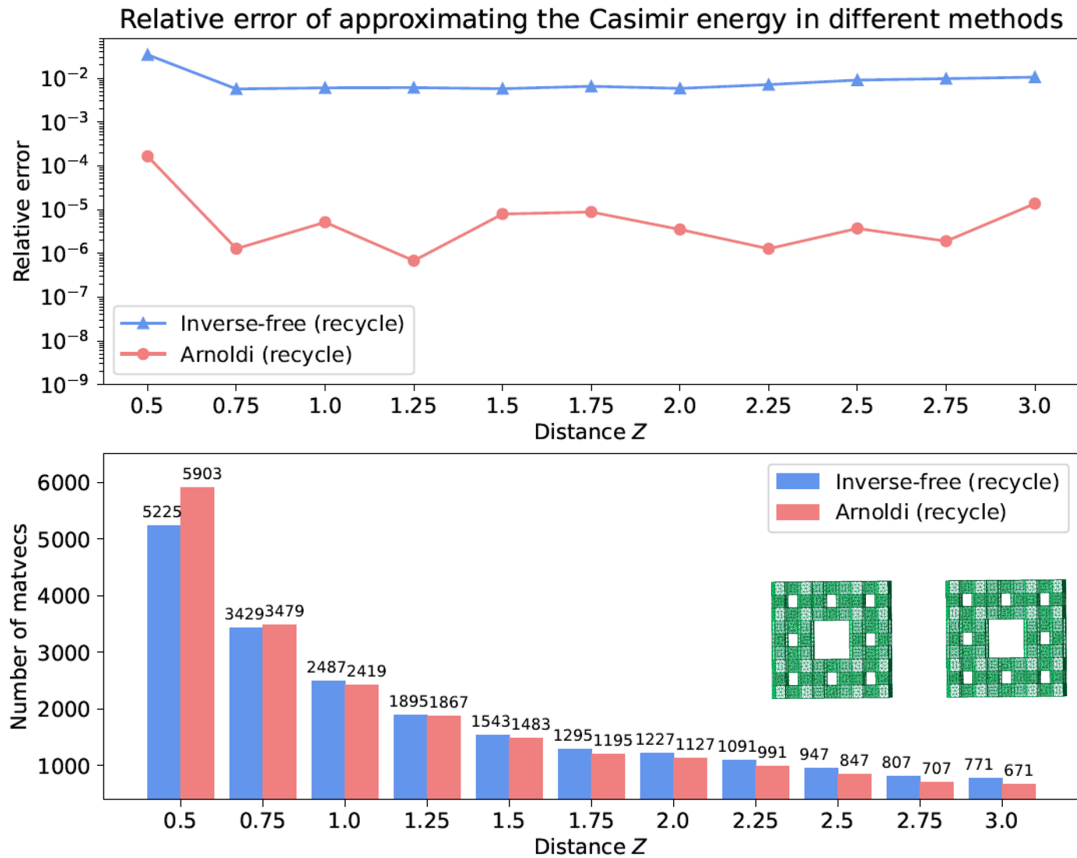
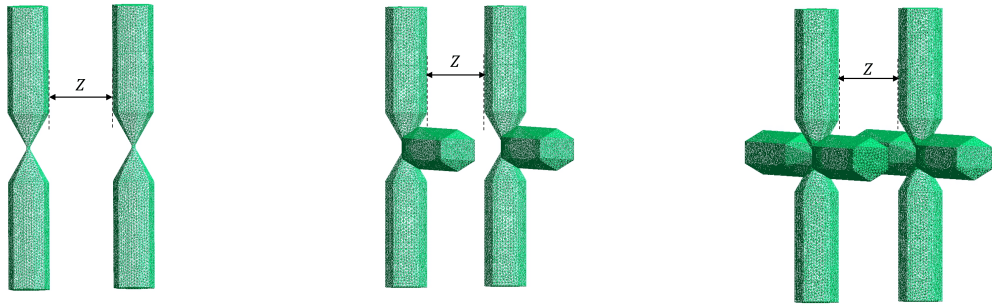


Figure 15: Menger sponges in Level 2's case: relative distance between the reference value (computed by Richardson extrapolation) with the estimates evaluated from the standard Arnoldi method with subspace recycled (solid red circles) and inverse-free Krylov subspace method with subspace recycled (solid blue triangles). The dimension of the Krylov subspace is $m = 100$.

In the next example, the scatterers are ice crystals with different number of branches ranging from 2 to 6 (see Figure 16).



(a) Two branches: $\dim(V_{ik}) = 8792$
 N^o of elements on both grids = 17576

(b) Three branches: $\dim(V_{ik}) = 13104$
 N^o of elements on both grids = 26200

(c) Four branches: $\dim(V_{ik}) = 17554$
 N^o of elements on both grids = 35100



(d) Five branches: $\dim(V_{ik}) = 21950$
 N^o of elements on both grids = 43900

(e) Six branches: $\dim(V_{ik}) = 26262$
 N^o of elements on both grids = 52556

Figure 16: Ice crystals with different number of branches

Normalized Casimir energy in ice crystals' case					
Distance	2-branches	3-branches	4-branches	5-branches	6-branches
0.5	0.04112	0.05989	0.07848	0.07873	0.01128
0.75	0.01499	0.02184	0.02855	0.02873	0.005017
1.0	0.007403	0.01080	0.01412	0.01428	0.002965
1.25	0.004242	0.006198	0.008113	0.008242	0.001985
1.5	0.002672	0.003905	0.005117	0.005223	0.001427
1.75	0.001797	0.002624	0.003442	0.003530	0.001074
2.0	0.001268	0.001849	0.002428	0.002501	0.0008357
2.25	0.0009288	0.001353	0.001776	0.001839	0.0006664
2.5	0.0007007	0.001019	0.001338	0.001391	0.0005410
2.75	0.0005413	0.0007863	0.001033	0.001078	0.0004469
3.0	0.0004270	0.0006188	0.0008134	0.0008526	0.0003741

Table 8: Normalized Casimir energy in 2- to 6-branched ice crystals' case

The integrand value of Casimir integral formula

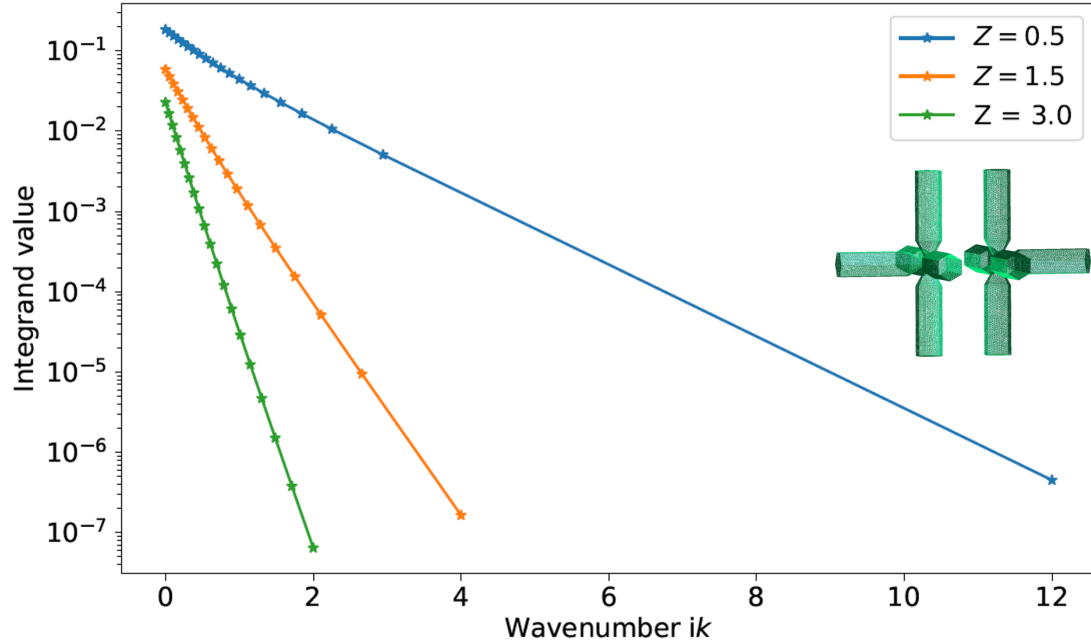


Figure 17: The integrand of the Casimir energy between two five-branches ice crystals with distance $Z = 0.5, 1.5$ and 3.0 .

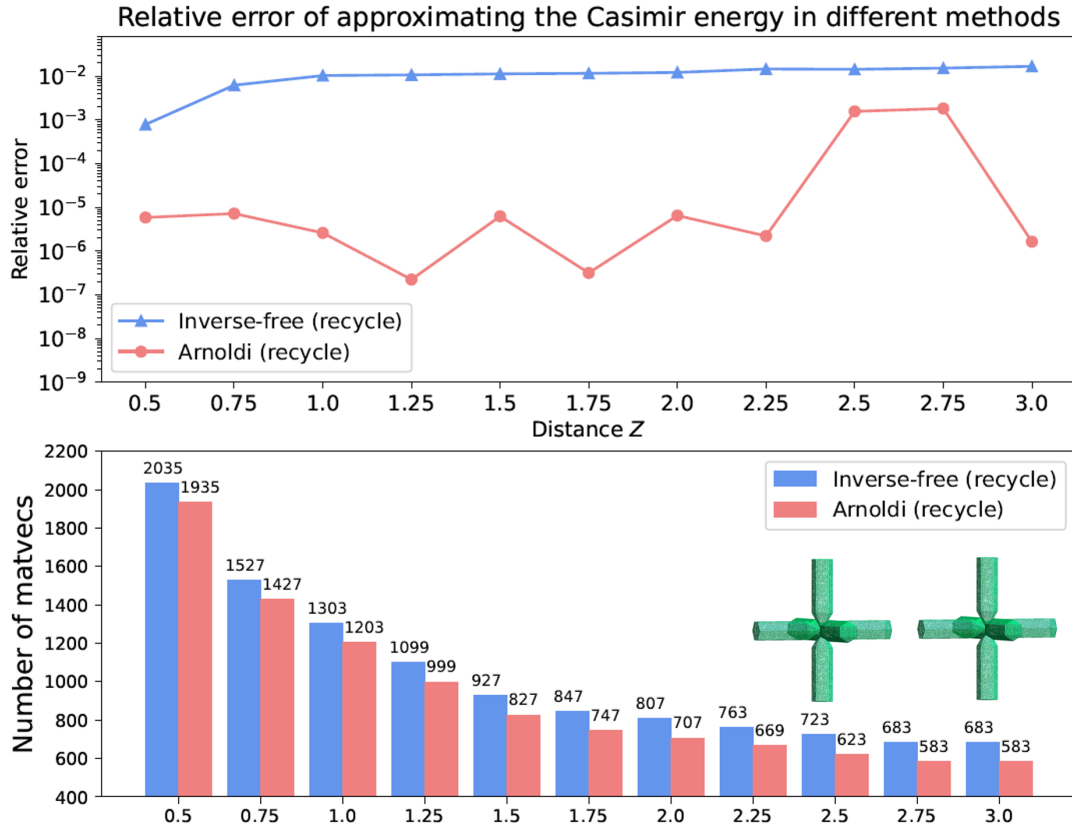


Figure 18: Six-branches ice crystals' case: relative distance between the reference value (computed by Richardson extrapolation) with the estimates evaluated from the standard Arnoldi method with subspace recycled (solid red circles) and inverse-free Krylov subspace method with subspace recycled (solid blue triangles). The dimension of the Krylov subspace is $m = 100$.

It is not hard to imagine that the Casimir energy would be different after the scatterers rotate while keeping the distance between them unchanged. Therefore, in the last example, we would see how the Casimir energy between two identical ellipsoids changes as one of the ellipsoids rotates.

In Figure 19a, the above ellipsoid is centering at $(0, 0, 0)$ and the below one is centering at $(0, 0, -(0.5 + 0.5 + Z))$, where Z is the distance between these two ellipsoids. Without rotation, the Casimir energy between them with different distance Z is plotted in Figure 20a.

To explore how the rotation affects the change of the Casimir energy, one can always keep one ellipsoid fixed and rotate the other one. The Figure 19b and 19c describe the case when one of the ellipsoids rotates around z - and x -axis, respectively. From the Figure 20b, the Casimir energy changes periodically since we rotate one ellipsoid around z - or x -axis by 360 degrees.

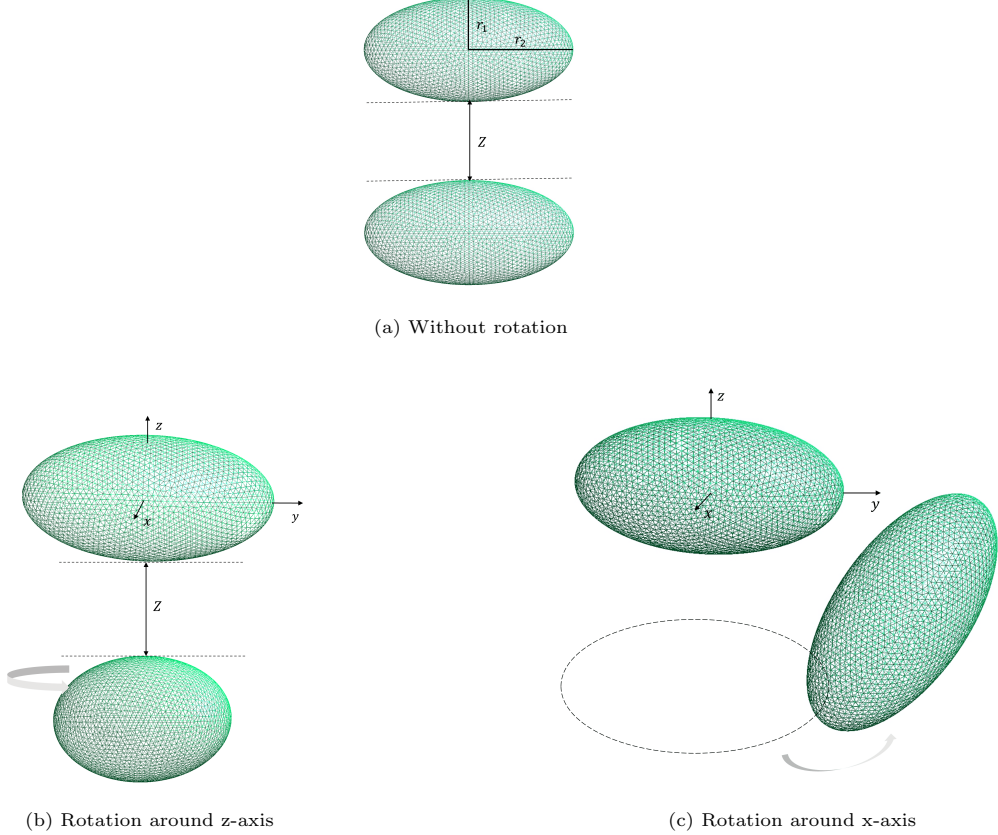
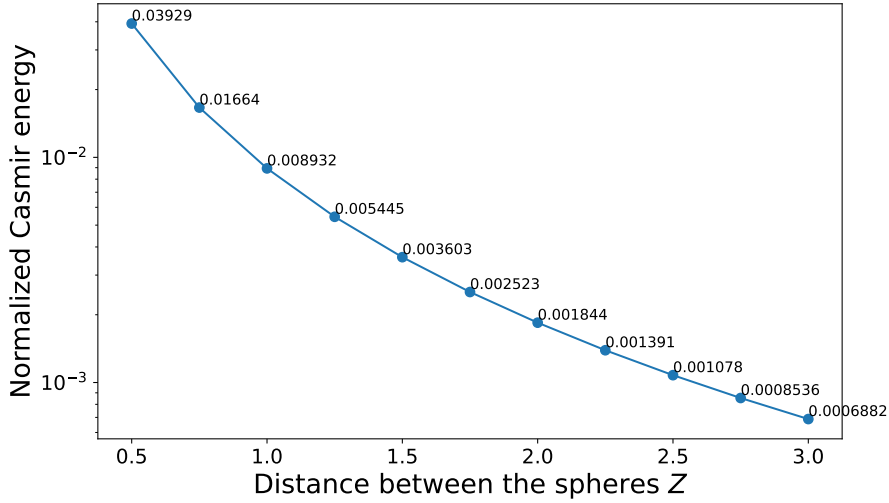


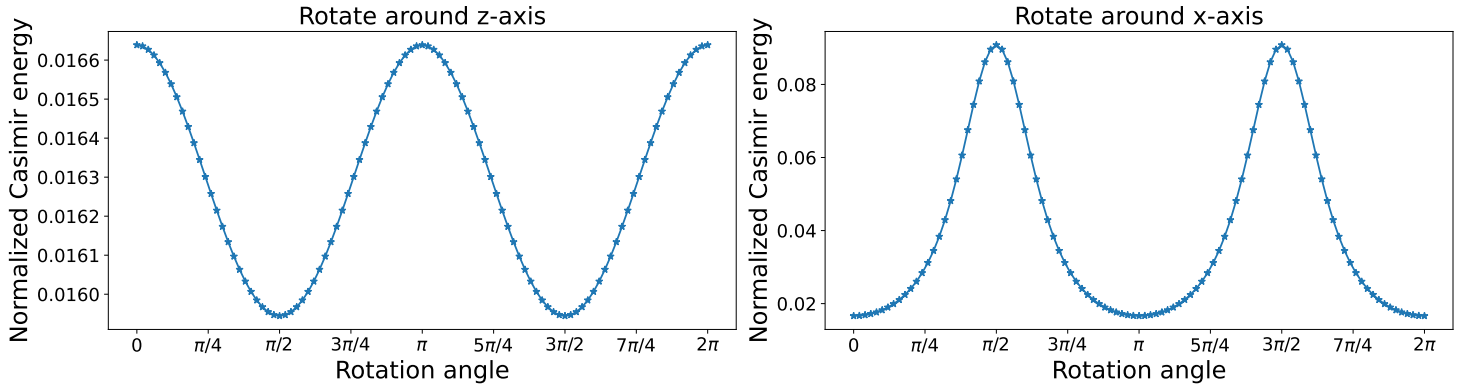
Figure 19: Two ellipsoids with or without rotation: when $h_{\text{fine}} = 0.05$, $\dim(V_{ik}) = 5517$; $h_{\text{coarse}} = 0.1$, $\dim(V_{ik}) = 1498$. The principal semi-axes of two ellipsoids are $r_1 = 0.5$ and $r_2 = 1.0$.

Casimir energy between two ellipsoids without rotations



(a) Casimir energy between two ellipsoids with different distances

Casimir energy between two ellipsoids with rotations



(b) Casimir energy when one of the ellipsoids rotates

Figure 20: The dependence of the Casimir energy and rotation angle of one of the ellipsoids.

Now, consider 4 ellipsoids located on the vertices of a regular tetrahedron with edge length $l = 2$ (Figure 21) and the principal semi-axes of all these ellipsoids are $r_1 = 0.6$ and $r_2 = 0.3$. Figure 21b and Figure 21c show the rotation of the ellipsoids inwards and outwards 360 degrees towards the centroid of this tetrahedron, separately. Afterwards, in order to use the Richardson extrapolation method to estimate the Casimir energy, we evaluate the integral (5) with the grid size set as $h_{\text{fine}} = 0.05$ and $h_{\text{coarse}} = 0.03$. Note that the number of the scatterers has increased to four, the matrices V_{ik} and \tilde{V}_{ik} have become to 4 by 4 block and diagonal block matrix, respectively. From the Figure 22, it shows that the Casimir energy between these four ellipsoids changes periodically with the rotation.

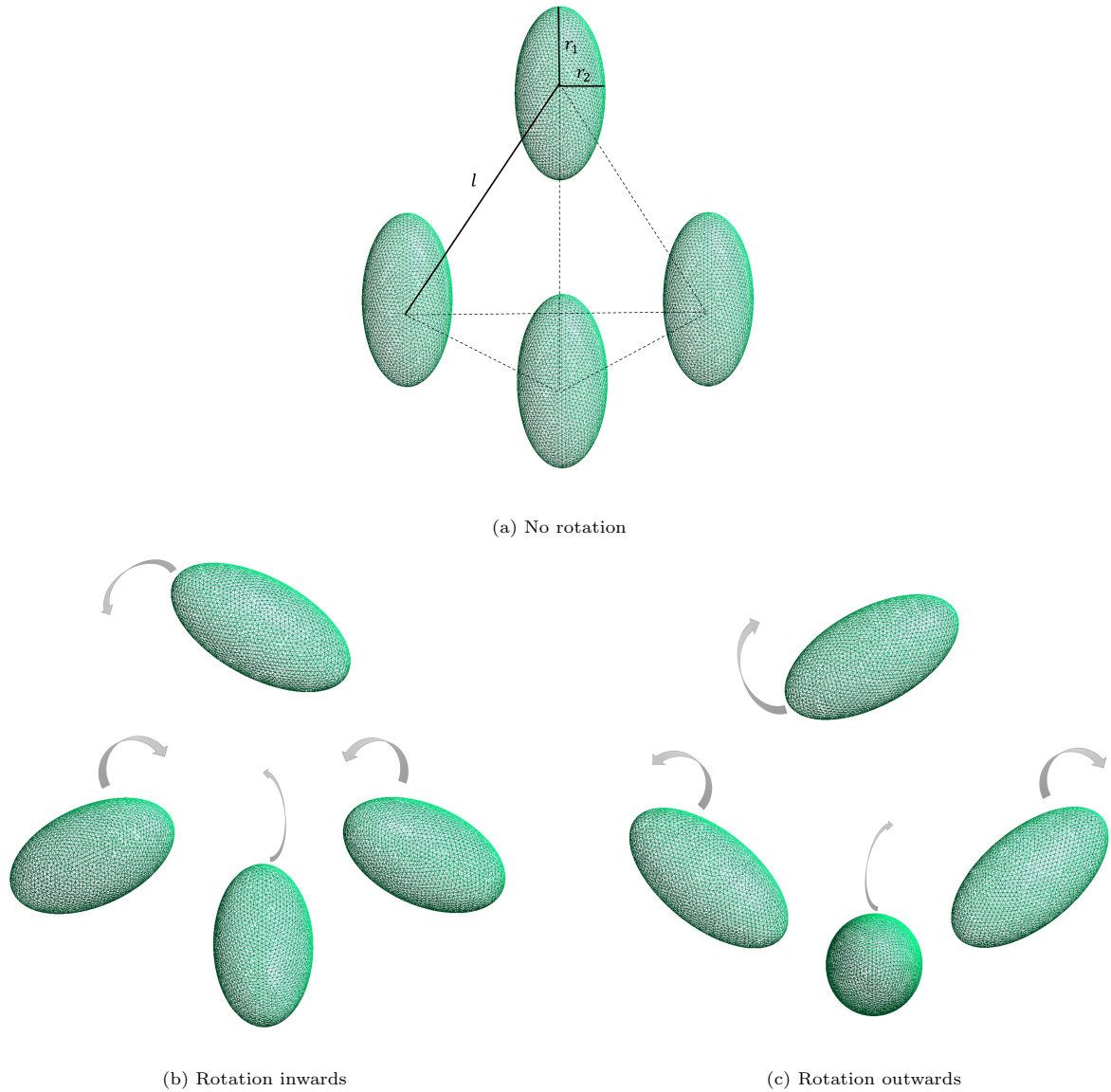


Figure 21: Four ellipsoids with or without rotations: when $h_{\text{fine}} = 0.03$, $\dim(V_{ik}) = 11024$; $h_{\text{coarse}} = 0.05$, $\dim(V_{ik}) = 4160$. The principal semi-axes of these ellipsoids are $r_1 = 0.6$ and $r_2 = 0.3$ and they locate on the vertices of a regular octahedron with edge length $l = 2$.

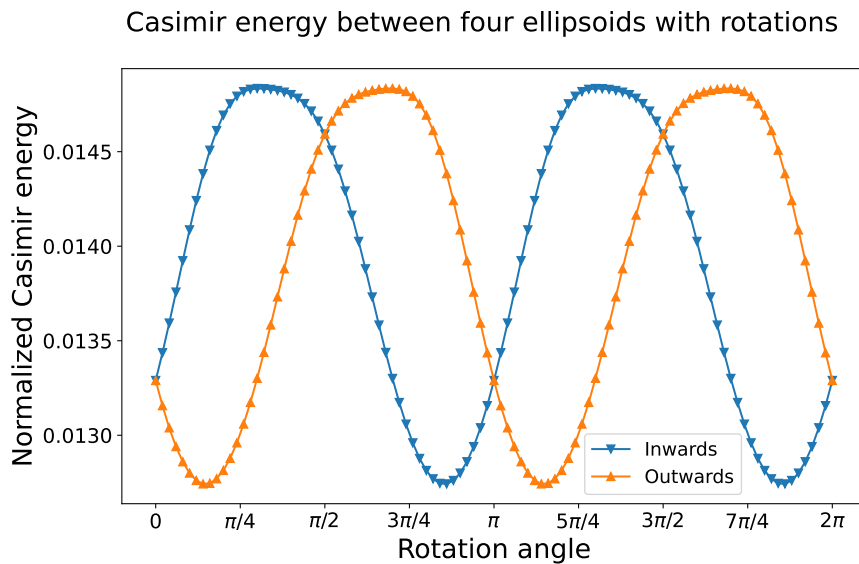


Figure 22: The dependence of the Casimir energy and rotation angle of one of the ellipsoids. Inwards towards the centroid case (solid blue square). Outwards towards the centroid case (solid orange triangle).

The scatterers of the last example are described inside the Figure 23. These six ellipsoids locate on the vertices of a regular octahedron with edge length $l = 2$ and again the principal semi-axes of all these ellipsoids are $r_1 = 0.6$ and $r_2 = 0.3$ (shown in the Figure 23). This time, the ellipsoids rotate inwards and outwards 360 degrees towards the centroid of this octahedron (Figure 23b and Figure 23c). By closely looking at these two rotation figures, we can notice that Figure 23b can be obtained by rotating Figure 23c 180 degrees. Therefore, the Casimir energies for the inwards and outwards cases are the same. Figure (24) shows how the Casimir energy changes among these six ellipsoids as they rotate.

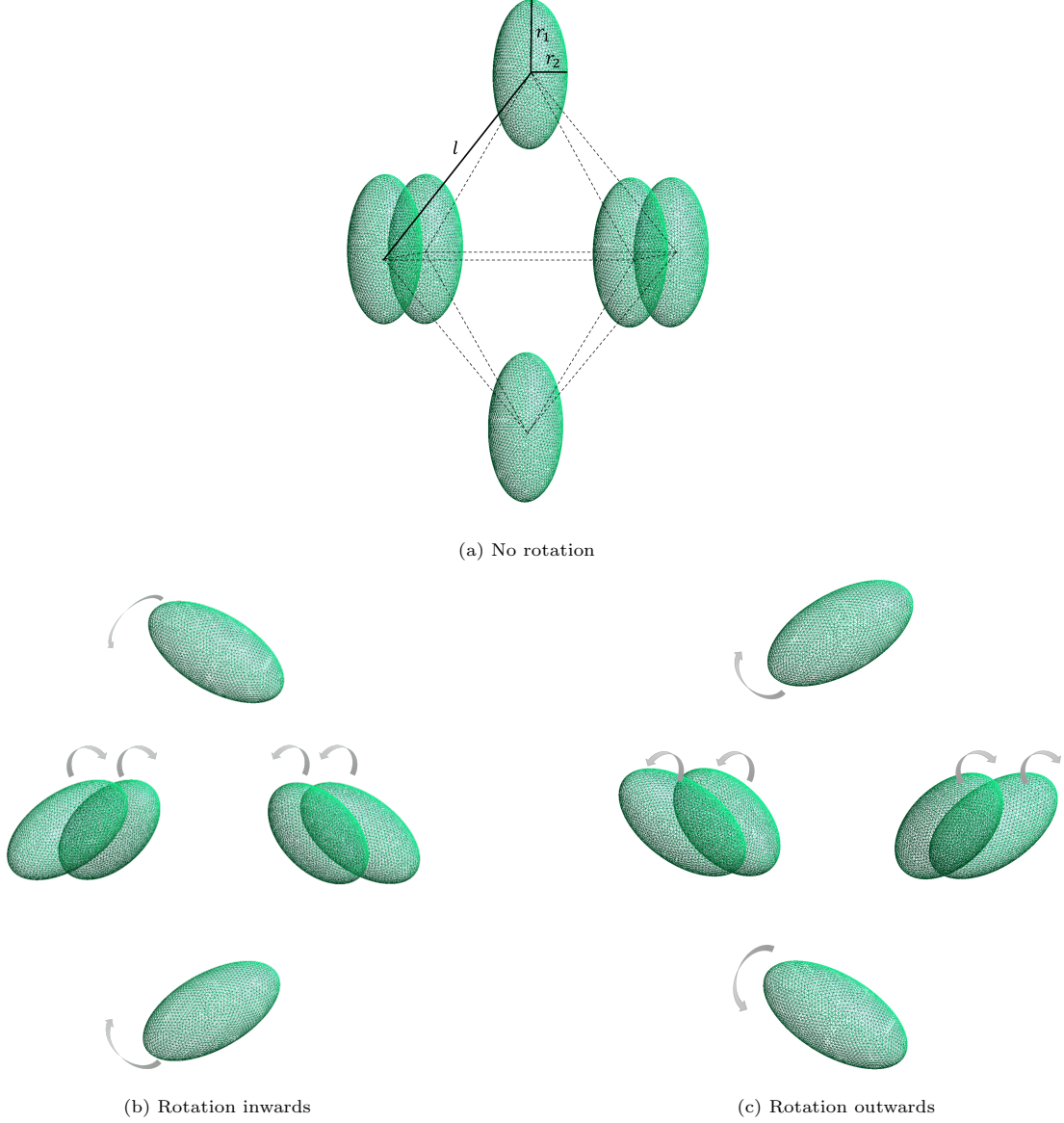


Figure 23: Six ellipsoids with or without rotations: when $h_{\text{fine}} = 0.03$, $\dim(V_{ik}) = 16536$; $h_{\text{coarse}} = 0.05$, $\dim(V_{ik}) = 6240$. The principal semi-axes of these ellipsoids are $r_1 = 0.6$ and $r_2 = 0.3$ and they locate on the vertices of a regular octahedron with edge length $l = 2$.

Casimir energy between six ellipsoids with rotations

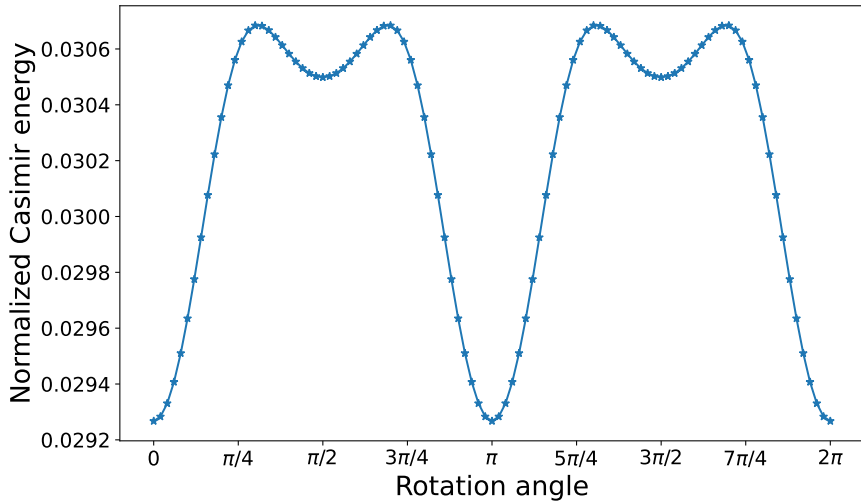


Figure 24: The dependence of the Casimir energy and rotation angle of one of the ellipsoids.

6. Conclusion

We have introduced the representation of the Casimir energy in terms of the boundary integral operators and its connection to the relative Krein spectral shift function. With the rigorous proof of the Casimir energy formula, we present several numerical methods for the calculation of the Casimir energy by applying the spectral properties of the Galerkin discretized form of the boundary integral operators. These methods are based on the classical Krylov subspace projection methods and subspaces recycled also significantly reduce the number of the matrix-vector multiplications and speed up the calculations for large-scale practical problems.

For the future work, we will consider the calculation of the Casimir energy in electromagnetic scattering and apply the fast multipole method (FMM) when assembling the boundary operator with a shorter assembly time but slower matvecs and compare with the method without implementing FMM.

References

- [1] H. B. Casimir, On the attraction between two perfectly conducting plates, in: Proc. Kon. Ned. Akad. Wet., Vol. 51, 1948, p. 793.
- [2] M. J. Sparnaay, Measurements of attractive forces between flat plates, Physica 24 (6-10) (1958) 751–764.
- [3] S. K. Lamoreaux, Demonstration of the casimir force in the 0.6 to 6 μ m range, Physical Review Letters 78 (1) (1997) 5.
- [4] T. Ederth, Template-stripped gold surfaces with 0.4-nm rms roughness suitable for force measurements: Application to the casimir force in the 20–100-nm range, Physical Review A 62 (6) (2000) 062104.
- [5] G. Bressi, G. Carugno, R. Onofrio, G. Ruoso, Measurement of the casimir force between parallel metallic surfaces, Physical review letters 88 (4) (2002) 041804.
- [6] D. Krause, R. Decca, D. López, E. Fischbach, Experimental investigation of the casimir force beyond the proximity-force approximation, Physical review letters 98 (5) (2007) 050403.
- [7] H. B. Chan, Y. Bao, J. Zou, R. Cirelli, F. Klemens, W. Mansfield, C. Pai, Measurement of the casimir force between a gold sphere and a silicon surface with nanoscale trench arrays, Physical review letters 101 (3) (2008) 030401.

- [8] M. Bordag, U. Mohideen, V. M. Mostepanenko, New developments in the casimir effect, Physics reports 353 (1-3) (2001) 1–205.
- [9] M. Bordag, G. L. Klimchitskaya, U. Mohideen, V. M. Mostepanenko, Advances in the Casimir effect, Vol. 145, OUP Oxford, 2009.
- [10] E. Elizalde, A. Romeo, Expressions for the zeta-function regularized casimir energy, Journal of mathematical physics 30 (5) (1989) 1133–1139.
- [11] E. Elizalde, A. Romeo, Heat-kernel approach to the zeta-function regularization of the casimir energy for domains with curved boundaries, International Journal of Modern Physics A 5 (09) (1990) 1653–1669.
- [12] K. Kirsten, Spectral functions in mathematics and physics, Chapman and Hall/CRC, 2001.
- [13] I. E. Dzyaloshinskii, E. M. Lifshitz, L. P. Pitaevskii, The general theory of van der waals forces, Advances in Physics 10 (38) (1961) 165–209.
- [14] L. S. Brown, G. J. Maclay, Vacuum stress between conducting plates: an image solution, Physical Review 184 (5) (1969) 1272.
- [15] D. Deutsch, P. Candelas, Boundary effects in quantum field theory, Physical Review D 20 (12) (1979) 3063.
- [16] B. S. Kay, Casimir effect in quantum field theory, Physical Review D 20 (12) (1979) 3052.
- [17] G. Scharf, W. Wreszinski, On the casimir effect without cutoff, Foundations of Physics Letters 5 (5) (1992) 479–487.
- [18] S. A. Fulling, et al., Vacuum energy as spectral geometry, SIGMA. Symmetry, Integrability and Geometry: Methods and Applications 3 (2007) 094.
- [19] M. Renne, Microscopic theory of retarded van der waals forces between macroscopic dielectric bodies, Physica 56 (1) (1971) 125–137.
- [20] G. Bimonte, T. Emig, M. Kardar, M. Krüger, Nonequilibrium fluctuational quantum electrodynamics: Heat radiation, heat transfer, and force, Annual Review of Condensed Matter Physics 8 (2017) 119–143.
- [21] T. Emig, N. Graham, R. Jaffe, M. Kardar, Casimir forces between arbitrary compact objects, Physical review letters 99 (17) (2007) 170403.
- [22] T. Emig, R. Jaffe, M. Kardar, A. Scardicchio, Casimir interaction between a plate and a cylinder, Physical review letters 96 (8) (2006) 080403.
- [23] T. Emig, R. Jaffe, Casimir forces between arbitrary compact objects, Journal of Physics A: Mathematical and Theoretical 41 (16) (2008) 164001.
- [24] T. Emig, N. Graham, R. Jaffe, M. Kardar, Casimir forces between compact objects: The scalar case, Physical Review D 77 (2) (2008) 025005.
- [25] O. Kenneth, I. Klich, Opposites attract: A theorem about the casimir force, Physical review letters 97 (16) (2006) 160401.
- [26] O. Kenneth, I. Klich, Casimir forces in a t-operator approach, Physical Review B 78 (1) (2008) 014103.

- [27] K. A. Milton, J. Wagner, Multiple scattering methods in casimir calculations, *Journal of Physics A: Mathematical and Theoretical* 41 (15) (2008) 155402.
- [28] S. J. Rahi, T. Emig, N. Graham, R. L. Jaffe, M. Kardar, Scattering theory approach to electrodynamic casimir forces, *Physical Review D* 80 (8) (2009) 085021.
- [29] F. Hanisch, A. Strohmaier, A. Waters, A relative trace formula for obstacle scattering, arXiv preprint arXiv:2002.07291 (2020).
- [30] A. Strohmaier, The classical and quantum photon field for non-compact manifolds with boundary and in possibly inhomogeneous media, *Communications in Mathematical Physics* 387 (3) (2021) 1441–1489.
- [31] Y.-L. Fang, A. Strohmaier, A mathematical analysis of casimir interactions i: The scalar field, in: *Annales Henri Poincaré*, Springer, 2021, pp. 1–51.
- [32] Y.-L. Fang, A. Strohmaier, Singularity traces in obstacle scattering and the poisson relation for the relative trace, arXiv preprint arXiv:2104.01017 (2021).
- [33] M. W. Scroggs, T. Betcke, E. Burman, W. Šmigaj, E. van't Wout, Software frameworks for integral equations in electromagnetic scattering based on calderón identities, *Computers & Mathematics with Applications* 74 (11) (2017) 2897–2914.
- [34] P. Waterman, New formulation of acoustic scattering, *The journal of the acoustical society of America* 45 (6) (1969) 1417–1429.
- [35] M. Ganesh, S. C. Hawkins, A far field based t-matrix method for three dimensional acoustic scattering, *ANZIAM Journal* 50 (2008) 121–136.
- [36] Y.-L. Fang, A. Strohmaier, Trace singularities in obstacle scattering and the poisson relation for the relative trace, *Annales mathématiques du Québec* 46 (1) (2022) 55–75.
- [37] Y. Nakatsukasa, Off-diagonal perturbation, first-order approximation and quadratic residual bounds for matrix eigenvalue problems, in: *International Workshop on Eigenvalue Problems: Algorithms, Software and Applications in Petascale Computing*, Springer, 2015, pp. 233–249.
- [38] G. H. Golub, Q. Ye, An inverse free preconditioned krylov subspace method for symmetric generalized eigenvalue problems, *SIAM Journal on Scientific Computing* 24 (1) (2002) 312–334.
- [39] J. H. Money, Q. Ye, Algorithm 845: Eigifp: A matlab program for solving large symmetric generalized eigenvalue problems, *ACM Transactions on Mathematical Software (TOMS)* 31 (2) (2005) 270–279.
- [40] Y. Saad, *Numerical methods for large eigenvalue problems: revised edition*, SIAM, 2011.